

zoomies: A tool to infer stellar age from vertical action in *Gaia* data

SHEILA SAGEAR ^{1,2} ADRIAN M. PRICE-WHELAN ¹ SARAH BALLARD ² YUXI (LUCY) LU ³ RUTH ANGUS ^{3,1} AND
DAVID W. HOGG ^{4,5,1}

¹*Center for Computational Astrophysics, Flatiron Institute, 162 5th Avenue, Manhattan, NY, USA*

²*Department of Astronomy, University of Florida, 211 Bryant Space Science Center, Gainesville, FL 32611*

³*American Museum of Natural History, Central Park West, Manhattan, NY, USA*

⁴*Center for Cosmology and Particle Physics, Department of Physics, New York University, 726 Broadway, New York, NY 10003, USA*

⁵*Max-Planck-Institut für Astronomie, Königstuhl 17, D-69117 Heidelberg, Germany*

ABSTRACT

Stellar age measurements are fundamental to understanding a wide range of astronomical processes, including galactic dynamics, stellar evolution, and planetary system formation. However, extracting age information from main-sequence stars is complicated, with techniques often relying on age proxies in the absence of direct measurements. The *Gaia* data releases have enabled detailed studies of the dynamical properties of stars within the Milky Way, offering new opportunities to understand the relationship between stellar age and dynamics. In this study, we leverage high-precision astrometric data from *Gaia* DR3 to construct a stellar age prediction model based only on stellar dynamical properties; namely, the vertical action. We calibrate two distinct, hierarchical stellar age–vertical action relations, first employing asteroseismic ages for red giant branch stars, then isochrone ages for main-sequence turn-off stars. We describe a framework called **zoomies** based on this calibration, by which we can infer ages for any star given its vertical action. This tool is open-source and intended for community use. We compare dynamical age estimates from **zoomies** with age measurements from open clusters and asteroseismology. We use **zoomies** to generate and compare dynamical age estimates for stars from the Kepler, K2, and TESS exoplanet transit surveys. While dynamical age relations are associated with large uncertainty, they are generally mass-independent and depend on homogeneously measured astrometric data. These age predictions are uniquely useful for large-scale demographic investigations, especially in disentangling the relationship between planet occurrence, metallicity, and age for low-mass stars.

Keywords: Stellar kinematics (1608), Stellar ages (1581), Galaxy dynamics (591), Exoplanets (498)

1. INTRODUCTION

The *Gaia* data releases (Prusti et al. 2016; Vallenari et al. 2023) have revolutionized our understanding of Galactic dynamics, along with stellar and planetary astronomy within a broader Galactic context. The motions of stars within the galaxy encode age information: generally speaking, older stars exhibit higher velocity dispersion or vertical action as a population (Wielen 1977; Rocha-Pinto et al. 2004; Almeida-Fernandes & Rocha-Pinto 2018). Historically speaking, low-mass dwarfs have been especially useful in calibrating stellar age and Galactic kinematics, by virtue of their long lifetimes (Reid et al. 1995; Faherty et al. 2009; Kiman et al. 2019; Angus et al. 2020; Popinchalk et al. 2021).

Understanding the ages of stars is key to understanding not only how stars themselves evolve, but also how galaxies evolve and how planetary systems behave over time. Stellar ages are particularly interesting for constraining the occurrence rate and evolution of planetary systems over time. Transit surveys enabled by NASA’s *Kepler* Mission (Borucki et al. 2010) and the Transiting Exoplanet Survey Satellite (*TESS*, Ricker et al. 2014) have discovered thousands of exoplanets in the past decade (Guerrero et al. 2021). The number of exoplanets known today has not only enabled the study of individual planets and systems, but also their ensemble properties. Here *Gaia* has also played a pivotal role by improving constraints on stellar properties (e.g. Fulton & Petigura 2018; Berger et al. 2020a, 2023) as well as linking planet occurrence and Galactic position or kinematics (Winter et al. 2020; Dai et al. 2021; Chen et al. 2021a; Longmore et al. 2021; Bashi & Zucker 2021; Zink et al. 2023). It is as-yet uncertain whether correlations between

planet occurrence and Galactic position are due to the Galactic environment directly (e.g. Cai et al. 2017; Ndugu et al. 2022) or reflect a separate, underlying relationship between planet occurrence and stellar metallicity or age (e.g. Nielsen et al. 2023).

Investigating how the orbits of planets evolve over time is key to fully understanding how they form, the dependence of planet properties on stellar properties (such as metallicity), and prospects for habitability. However, this investigation likely hinges on our knowledge of stellar age, which is notoriously difficult to constrain. A precise understanding of stellar age is even more elusive for the predominant exoplanet hosts, FGK-type dwarfs and (especially) M dwarfs. Small, rocky, habitable-zone exoplanets are abundant around the lowest-mass stars (e.g. Mulders et al. 2015) and relatively easy to observe using transit surveys due to their relatively large planet radius-stellar radius ratio (Tarter et al. 2007). Unfortunately, it is difficult to constrain ages for the lowest-mass stars because their lifetimes are often longer than the age of the universe (Choi et al. 2016). Isochrone grids are additionally an unreliable source of age measurements, as they often fail to reproduce empirical constraints for M dwarfs due to the presence of strong magnetic fields and starspots (Feiden & Chaboyer 2012; Boyajian et al. 2012; Mann et al. 2019).

Though measuring ages for low-mass stars is uniquely challenging, measuring ages for stars of any mass is non-trivial. Stellar ages cannot be directly measured; they can only be inferred using techniques such as comparing measured properties to isochrone models and asteroseismology (e.g. Karataş et al. 2005; Lebreton & Montalbán 2009; Silva Aguirre et al. 2015) or using empirical relations such as gyrochronology and age-activity relations (e.g. Barnes 2007; Soderblom et al. 1991; for review, Soderblom 2010). Recent studies such as Lu et al. (2021) also combine such empirical methods with certain stellar kinematic information. These quantities are associated with relative ages with varying levels of precision (e.g. Epstein & Pinsonneault 2013; Tayar et al. 2022). Additionally, the introduction of large-scale spectroscopic surveys including the RAdial Velocity Experiment (RAVE, Steinmetz et al. 2006), the Large Sky Area Multi-Object Fiber Spectroscopic Telescope (LAMOST, Zhao et al. 2012; Cui et al. 2012), the Galactic Archaeology with HERMES survey (GALAH, De Silva et al. 2015; Martell et al. 2017), and the Apache Point Observatory Galactic Evolution Experiment (APOGEE, Majewski et al. 2017) has delivered spectroscopic data for millions of stars. With these, several groups have recently attempted to obtain spectroscopic stellar ages (e.g. Queiroz et al. 2018, 2020, 2023; Mints & Hekker 2017, 2018).

We are motivated by the prospect of conducting large-scale demographic studies on how the orbital dynamics and properties of exoplanets change over time. We now have high-precision astrometric information from *Gaia* homogeneously derived for virtually every nearby star. With stellar parallax, proper motion, and radial velocity measured by *Gaia* along with some assumed potential model of the Milky Way, we can compute a star’s Galactic orbit. It has been established for decades that there is a relationship between the velocity dispersion of stars and age (the age–velocity dispersion relation, or AVR) (e.g. Strömberg 1946; Wielen 1977), and dynamical ages have shown potential in calibrating ages even for low-mass dwarf stars (e.g. Veyette & Muirhead 2018; Newton et al. 2018; Lu et al. 2024a,b). We leverage this nearly stellar-mass-independent Galactic orbit information to construct an age–Galactic orbit relation based on a calibration sample of stars with independently inferred ages.

We note that there is as yet no definite consensus on the dominant cause of the AVR. The AVR may be primarily driven by the orbital heating histories of stars, such that the orbits of older stars have been kinematically heated over time (Spitzer & Schwarzschild 1953). The effect of disk heating on the AVR has been studied through various N-body and cosmological simulations (Hänninen & Flynn 2002; Holmberg et al. 2007; House et al. 2011; Aumer et al. 2016; Grand et al. 2016). Alternatively, the AVR may be observed as a consequence of the birthplaces of stars in the galaxy over time. Older stars may have been born kinematically hotter than younger stars, which form with a smaller velocity dispersion at later times, following a so-called “upside-down” and “inside out” galactic assembly process (Bird et al. 2013, 2021). Indeed, there is evidence to suggest that both mechanisms may contribute significantly to the observed AVR (McCluskey et al. 2024). We acknowledge that if disk heating is the primary driver of the AVR, then mapping stellar age to galactic orbits will be weakly dependent on stellar mass. Even in this case, dynamically-derived stellar ages will still be far less dependent on stellar mass than e.g. ages from isochrones or asteroseismology. To account for this lack of consensus in the primary cause of the AVR, we call the dynamical age model “generally mass-independent”.

Though we cannot directly measure the ages of stars, these dynamical age estimates provide homogeneous age predictions for hundreds of millions of stars with a wide range of stellar masses and properties. Because these age predictions depend only on dynamical data and the physical assumptions of galactic dynamics, they can be measured independently from other stellar properties such as metallicity and stellar rotation. Such age measurements may enable

us to disentangle the relationship between stellar age, metallicity, and other processes of interest (such as exoplanet orbital dynamics).

Due to systematic offsets between different age-dating methods, it is preferable that age predictions for an entire sample of interest are determined using the same method. Most samples of homogeneously inferred stellar ages are small, especially for main-sequence stars; for example, there are only $\mathcal{O}(10^2)$ main-sequence stars with precise asteroseismic age measurements (Huber et al. 2013; Silva Aguirre et al. 2015). Most stellar age prediction methods also depend strongly on stellar mass, further limiting the available age samples within a certain stellar mass bin (Barnes 2007; Soderblom 2010). This method of deriving dynamical stellar ages is particularly useful because it can be used to generate age predictions for all stars with *Gaia* radial velocities in a homogeneous way for a wide range of stellar masses.

In this work, we introduce a fully dynamical stellar age–vertical action relation calibrated on independently-measured ages of red giant branch and main-sequence turn-off stars. We release the software used in this analysis as an open-source dynamical age prediction tool called **zoomies**. We validate and compare dynamical age predictions for stars with independent asteroseismic ages, open clusters, and the large stellar samples of the *Kepler*, K2 and *TESS* missions. This paper is organized as follows: in Section 2 we describe the stellar samples used in calibration and validation. In Section 3 we describe our methods, including calculating dynamical properties, hierarchical model construction, and model fitting. In Section 4, we discuss internal validation checks on the dynamical age model. In Section 5, we introduce the model as an open-source age prediction tool and discuss dynamical age predictions for external stellar samples. In Section 6, we discuss how our assumptions may affect our results, and we conclude in Section 7.

2. DATA

2.1. Calibration Samples

We construct and calibrate two models to predict stellar age from Galactic orbital quantities. We employ two samples of independently measured stellar ages to calibrate the models (the *Calibration Samples*). We use a set of 20,917 red giant branch stars with asteroseismic ages from Stokholm et al. (2023) (hereafter the red-giant calibration sample, or “RGB” sample). We use only the stars from Stokholm et al. (2023) that have radial velocities measured with *Gaia*. We separately use a set of 33,715 main-sequence turn-off stars from the APOGEE DR17 sample with ages derived with the Bayesian isochrone-fitting code StarHorse (Queiroz et al. 2023) (hereafter the main-sequence turn off calibration sample, or the “MSTO” sample). We take only stars labeled as main-sequence turn-off stars by Queiroz et al. (2023) and filter on the included age warning flag “age_inout” indicating significant differences between input and output $\log g$, T_{eff} , and median metallicity. Using these two stellar age calibration samples, we calibrate two distinct dynamical age models; with this, we demonstrate that all dynamical age models depend on the properties of the calibration sample, especially their $\ln J_z$ distribution (see Figure 4).

2.2. Prediction Sample

The *Prediction Samples* refer to the stellar samples we generate age predictions for. This potentially includes all *Gaia* stars with radial velocity measurements. In this paper, we perform a preliminary analysis using the subset of *Kepler*, K2, and *TESS* main-sequence target stars with *Gaia* DR3 radial velocity measurements. In Figure 1, we present a visual comparison of the RGB Sample, MSTO Sample, and the Prediction Sample including all stars with *Gaia* DR3 radial velocities. In the left panel, we show a color-magnitude diagram (CMD) of the three samples with *Gaia* $B_p - R_p$ color and absolute *Gaia* (G) magnitude calculated from the G-band mean magnitude and the *Gaia* parallax. In the right panel, we compare the vertical action distributions for each of the three samples.

Whether stellar age estimates are generated with model-dependent, empirical, or kinematically motivated methods, these ages will be dependent on the calibration sample used. Different age predictions will invariably be offset according to the samples used to calibrate the age prediction model. The dynamical age predictions we present are no different; the age–action relations will be best calibrated in the regions of $\ln J_z$ where the calibration samples lie. Unless the prediction sample of interest is comparable to the calibration sample in $\ln J_z$ space, dynamical ages should generally be treated as relative, rather than absolute, age predictions. We show in the right panel of Figure 1 that the $\ln J_z$ distribution of the least restrictive prediction sample (all stars with *Gaia* radial velocities) differs significantly from the $\ln J_z$ distribution of both the RGB and MSTO samples; in such cases, we warn that stellar ages should be interpreted more conservatively as relative ages. Even so, understanding relative stellar ages is useful in many contexts (e.g. for investigating the evolution of planetary systems over time), especially since dynamical ages are measured independently

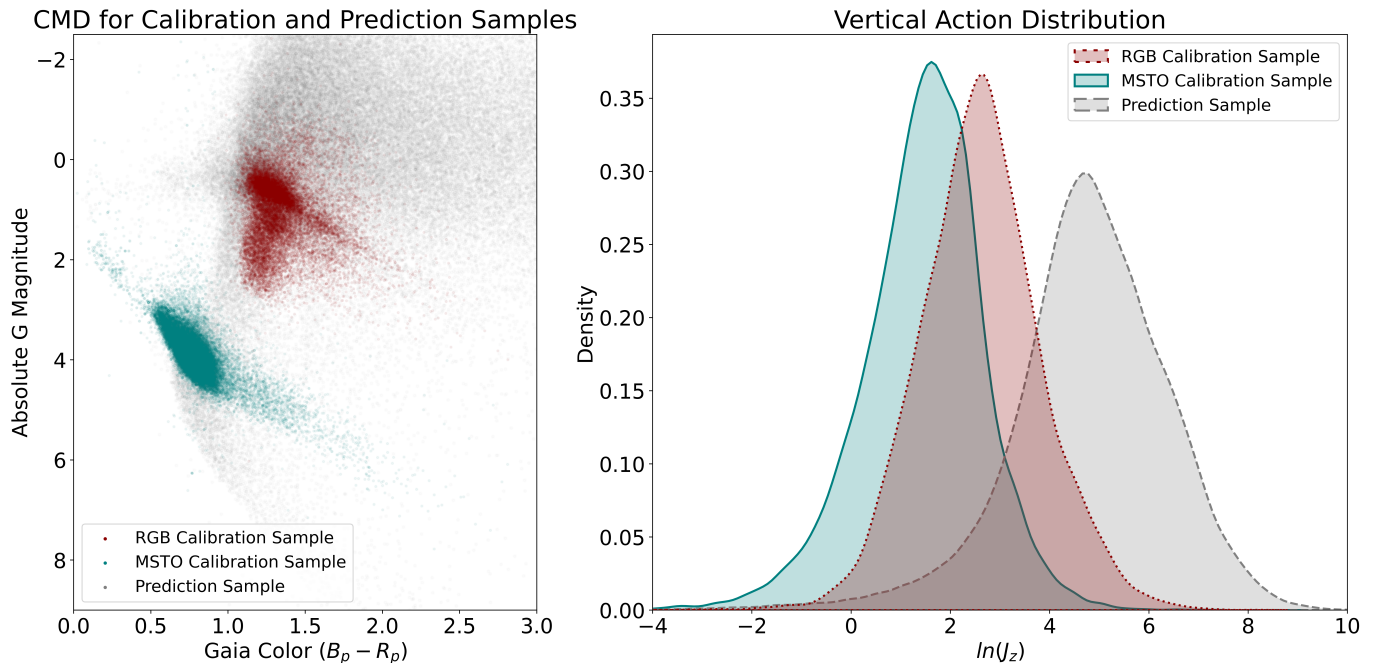


Figure 1. *Left:* Color-magnitude diagram of the RGB calibration sample (red), MSTO calibration sample (blue), and a representative prediction sample (gray). The representative prediction sample consists of the first 100,000 stars returned from a *Gaia* search excluding objects with no radial velocity measurements and $\varpi \leq 0$. *Right:* Vertical action distributions for the RGB (red), MSTO (blue) and representative *Gaia* sample (gray).

of most stellar properties and are available for very large samples of stars. We include more detailed discussions of this effect in Section 5.2.

3. METHODS

We construct a hierarchical Bayesian model to predict stellar age from Galactic orbital quantities. We first determine which Galactic orbital quantities to use. The ideal orbital quantity should be one that can be calculated homogeneously for a wide range of stars (given an assumed Milky Way potential model), and one that strongly correlates with stellar age. We could construct an age–vertical velocity (v_z) relation, but this would introduce a dependence on the temporal position of each star throughout its orbit. Any stars with wide galactic orbits in the z -direction that happen to be near the edge of their orbits would have a vertical velocity close to zero, which may unfairly bias their dynamical age prediction.

One alternative metric is an integral of motion that encodes time-independent information about a star’s galactic orbit. Given a static potential model of the galaxy, the action–angle variables are integrals of motion that describe an object’s orbit. Instead of vertical velocity, we elect to use an integral of motion that describes the extent of a star’s orbit independently from time: the vertical action, J_z . J_z is the integral of the vertical galactic position z vs. the vertical velocity v_z . J_z labels a star’s galactic orbit, no matter where a star happens to be in its orbit at the current moment. The vertical velocity v_z varies with time on the orbit, where J_z (along with z_{max} and other orbital constants of motion) would not. The vertical action is defined as

$$J_z = \frac{1}{2\pi} \oint dz v_z \quad (1)$$

where z describes the vertical position and v_z describes the vertical velocity of the object, and the integral is over the path of one full vertical orbit. Since J_z is independent of time, we contend that using J_z will produce a tighter age–galactic motion relation than using the vertical velocity alone. However, the J_z computations depend on the assumed galactic potential model and quality of the *Gaia* kinematic data in hand. We discuss the implications of considering only J_z in the age–action model (and not J_r , the radial action, or J_ϕ , the azimuthal action) in Section 6.2.

3.1. Calibrating the age–action relation

In this section, we describe the process of constructing and calibrating the age–action relation. We use an axisymmetric potential model of the Milky Way to compute the actions, implemented in the Python package `gala` (Price-Whelan 2017; Price-Whelan et al. 2020). This potential model includes a spherical galactic nucleus and bulge, a 3-component sum of Miyamoto-Nagai galactic disks (Miyamoto & Nagai 1975) representing an approximation to the potential from an exponential disk (Smith et al. 2015), and a spherical Navarro-Frenk-White dark matter halo model (Navarro et al. 1996). The disk model follows the galactic rotation curve from Eilers et al. (2019), and the vertical structure is set by the shape of the phase-space spiral in the solar neighborhood from Darragh-Ford et al. (2023). We describe a preliminary test on the impact of potential model choice on final stellar age predictions in Appendix B.

When calibrating the age– $\ln J_z$ model, we assume that the dynamical ages of stars are independent from stellar mass. We return to this assumption and discuss its implications in Section 6.1. For each star in each calibration sample, we first calculate the logarithm of the vertical action $\ln J_z$ given this Milky Way potential model. We calculate $\ln J_z$ from the *Gaia* proper motion, radial velocity, and using inverse parallax as the distance estimate. We use the `gala` software to make these calculations. We take the initial conditions given by the *Gaia* data and integrate each star’s orbit through time within the galactic potential model. We numerically integrate the orbits to calculate actions using the Staechel Fudge implementation in the `Agama` software (Vasiliev 2019). In both calibration samples, the errors in $\ln J_z$ are much smaller than the intrinsic variance in $\ln J_z$ (the average $\ln J_z$ uncertainty in both the RGB and MSTO samples is approximately 0.05, compared to a mean intrinsic variance of approximately 1.5), so we neglect the errors in $\ln J_z$. We performed a preliminary check on whether this intrinsic variance is correlated with any of several stellar parameters including stellar metallicity; $\log(g)$; T_{eff} ; distance; stellar mass, radius, and luminosity; α abundance; and ν_{max} . We found no evidence for correlations between the intrinsic variance and any of these stellar parameters. We provide further details of this check in Appendix C.

Next, we construct a hierarchical Bayesian model to describe the age– $\ln J_z$ relation. In this model, we wish to describe the log of the intrinsic variance (the squared uncertainty) in the age direction, $\ln V_\tau$, as a free parameter. Though we intend to construct a hierarchical model to predict stellar age given $\ln J_z$ (in other words, constructing a $P(\tau|\ln J_z)$ model), fitting a model to the age– $\ln J_z$ relation proves difficult when incorporating $\ln V_\tau$. Because the age– $\ln J_z$ relation is steep and has large scatter in the age direction, the value of the $\ln V_\tau$ free parameter balloons and fails to converge. To counteract this, we instead consider the $\ln J_z$ vs. age relation, $P(\ln J_z|\tau)$, where $\ln V_{\ln J_z}$ describes the intrinsic variance in the $\ln J_z$ direction. Once the $P(\ln J_z|\tau)$ model is calibrated, we obtain $P(\tau|\ln J_z)$ using a process we describe in detail in Section 3.2.

Since we calibrate the model on samples of main-sequence turn-off stars and red giant branch stars, the number density of stars along the age axis will reflect these samples. For example, the MSTO stellar sample has a high number density near 10 Gyr (see Figure 4, bottom left panel), which would unfairly bias the age prediction towards 10 Gyr when applied to other populations of stars with different number density distributions, such as main-sequence FGKM dwarfs. To counteract this effect, we estimate the stellar number density along the age axis $\lambda(\tau)$ as part of the age–action model, and we marginalize out $\lambda(\tau)$ when applying the model to other stars. This process enables us to apply only the slope and variance of the age–action model to other stellar samples, without also applying the calibration sample’s number density distribution. Accounting for the number density in this way produces a more generally applicable dynamical age prediction model.

Our method will not only require calibrating the age–action relationship, but also the calibration sample’s stellar number density in age, $\lambda(\tau)$. To estimate this, we include a Poisson likelihood component in the model likelihood function, similar in structure to the one used by Everall et al. (2022) in a different context. If the number density profile of stars along the age axis is $\lambda(\tau)$, we take the probability of drawing a population of stellar ages τ_i from $\lambda(\tau)$ to be the Poisson likelihood function (derived in Lombardi et al. 2013; Everall & Das 2020):

$$\ln \mathcal{L}_{\text{Poisson}} = \sum_{i=1}^N \ln \lambda(\tau_i) - \int \lambda(\tau) d\tau \quad (2)$$

In the hierarchical model, we describe the number density $\ln \lambda(\tau)$ as a third-degree spline defined between 0 and 14 Gyr. We add the Poisson likelihood factor into the complete model likelihood function. By independently fitting $\lambda(\tau)$ of the calibration sample in the age–action model, all other model parameters describing the age– $\ln J_z$ relation are not significantly influenced by the calibration sample’s non-uniform $\lambda(\tau)$. The $\lambda(\tau)$ distribution is specific to each

Table 1. Dynamical age–action model parameters

Parameter	Prior	Description
$\ln V_{\ln J_z}$	$\mathcal{N}(9, 5)$	Log of intrinsic variance
$V_{\ln J_z}$	Deterministic	Intrinsic variance
$t_{\tau(\ln J_z)}$	Fixed	Knot vector for $\tau(\ln J_z)$ spline, where $t_{\tau(\ln J_z)} = (t_{\tau(\ln J_z),1} \dots t_{\tau(\ln J_z),5})$
$\mathcal{S}(t_{\tau(\ln J_z)})$	$\mathcal{U}(0, 5)$	Knot values for $\tau(\ln J_z)$ spline, defined at each point in the knot vector $t_{\tau(\ln J_z)}$
$t_{\ln \lambda(\tau)}[\star]$	Fixed	Knot vector for $\ln \lambda(\tau)$ spline, where $t_{\ln \lambda(\tau)} = (t_{\ln \lambda(\tau),1} \dots t_{\ln \lambda(\tau),15})$
$\mathcal{S}(t_{\ln \lambda(\tau)})[\star]$	$\mathcal{U}(-10, 15)$	Knot values for $\ln \lambda(\tau)$ spline, defined at each point in the knot vector $t_{\ln \lambda(\tau)}$
$\ln \lambda(\tau)[\star]$	Observed	Log of stellar number density
τ	Observed	Stellar age
$\ln J_{z,pred}$	Observed	Predicted $\ln J_z$

NOTE—The priors listed for the spline knot values $\mathcal{S}(t_{\tau(\ln J_z)})$ and $\mathcal{S}(t_{\ln \lambda(\tau)})$ apply independently for each knot. A graphical model representation of the model is shown in Figure 2.

NOTE— $[\star]$: We fit $\lambda(\tau)$ in the dynamical age model, but we do not apply $\lambda(\tau)$ to generate dynamical age predictions for the prediction sample. We ignore these parameters when we apply the calibrated model to a prediction sample of stars.

calibration sample and is dependent on stellar mass, selection functions, and any number of other factors; we do not want the $\lambda(\tau)$ distribution of the calibration sample to affect the prediction sample’s dynamical age estimates. By fitting the calibration sample’s $\lambda(\tau)$ distribution and ignoring it when using the age– $\ln J_z$ model to generate age predictions for other stars, we minimize the risk of the calibration sample’s unique $\lambda(\tau)$ distribution affecting dynamical age estimates for other stars.

Finally, we model the $\ln J_z$ –age slope as a monotonic quadratic spline (a quadratic spline that must increase at each successive knot value).

We summarize the model fixed and free parameters here. The knot locations of the $\tau(\ln J_z)$ monotonic spline, $t_{\tau(\ln J_z)}$, are fixed at every 3.75 Gyr between -1 and 14 Gyr. The knot locations of the $\ln \lambda(\tau)$ third-degree spline, $t_{\ln \lambda(\tau)}$, are fixed at every 1 Gyr between -1 and 14 Gyr. The model free parameters include the knot values of the $\tau(\ln J_z)$ monotonic spline $\mathcal{S}(t_{\tau(\ln J_z)})$, the knot values of the $\ln \lambda(\tau)$ third-degree spline $\mathcal{S}(t_{\ln \lambda(\tau)})$, and the intrinsic variance $\ln V_{\ln J_z}$. We show the graphical model representation of this model in Figure 2. A list of the model free and fixed parameters is provided in Table 1. The model parameters associated with $\ln \lambda(\tau)$ which are ignored when using the model to generate age predictions for other stars are marked with “[\star]”.

We generate two mean posterior age– J_z relations: one using the red-giant branch star calibration age sample and one using the main-sequence turn off star calibration age sample. For each calibration sample, we sampled the free parameters using No U-Turn Sampling (Homan & Gelman 2014) with the Python package numptro (Phan et al. 2019; Bingham et al. 2019) with chains of 2,000 draws each. We use 2,000 tuning steps for each fit. To check for convergence, we calculate the Gelman-Rubin \hat{r} summary statistic for each model free parameter (Gelman & Rubin 1992). The \hat{r} statistic checks for convergence by comparing the level of variation among multiple MCMC chains. If the sampler successfully converged, \hat{r} is expected to be within 0.1 of 1. For both the RGB and MSTO models, all free parameters converged with $1.00 < \hat{r} < 1.05$.

3.2. Generating stellar age predictions

Given a value of $\ln J_z$, we use the calibrated age–vertical action relation to predict an age probability distribution. When using the mean posterior age– $\ln J_z$ model to predict ages for stars with $\ln J_z$, we ignore the number density in age. In other words, we consider only the mean and intrinsic variance of the age– $\ln J_z$ relation, and we do not consider the number density in age of the calibration samples when generating stellar age predictions.

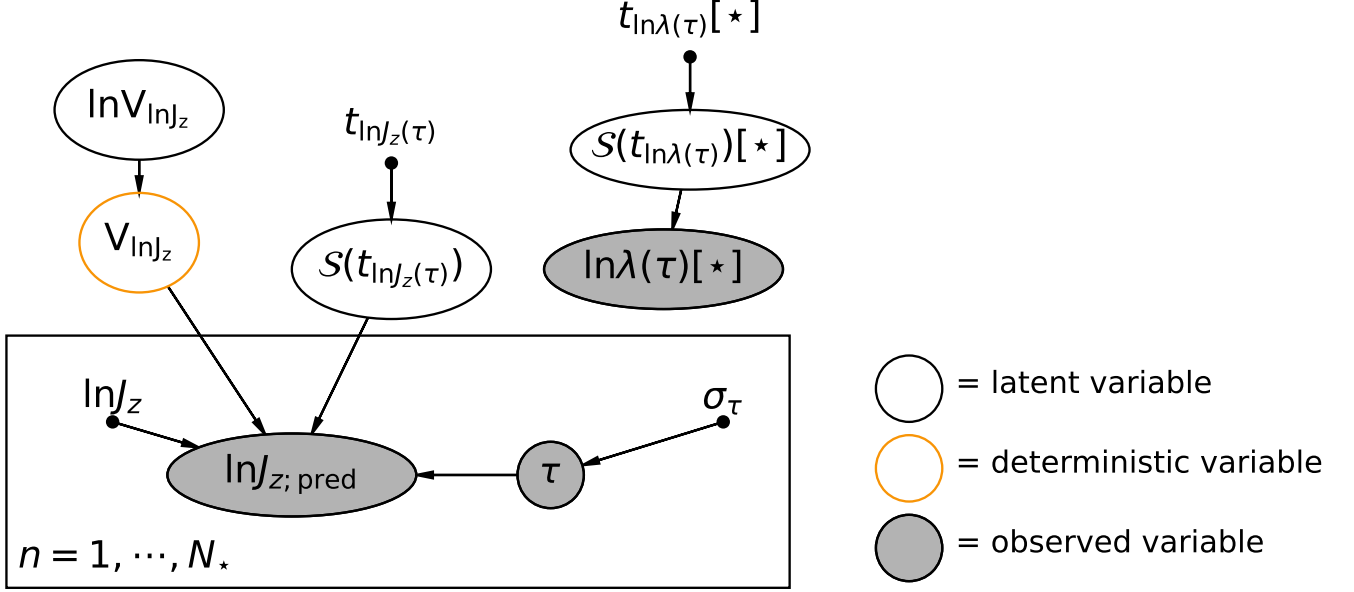


Figure 2. Graphical model representation of the hierarchical Bayesian stellar age– $\ln J_z$ model. $t_{\tau(\ln J_z)}$ and $t_{\ln \lambda(\tau)}$ refer to the fixed spline knot vectors for the $\tau(\ln J_z)$ and $\ln \lambda(\tau)$ splines, respectively, and $\mathcal{S}(t_{\tau(\ln J_z)})$ and $\mathcal{S}(t_{\ln \lambda(\tau)})$ represent the associated knot value free parameters. A list of the model parameters and their priors is given in Table 1. As in Table 1, “[*]” denotes a stellar number density model parameter that we ignore when we apply the calibrated model to a prediction sample of stars.

Due to the calibration samples’ large scatter on the age axis, we construct the age–action model to find $P(\ln J_z | \tau)$, as described in Section 3.1. In order to use this model to predict age from $\ln J_z$, we adjust this model to find $P(\tau | \ln J_z)$. We invoke Bayes’ theorem:

$$P(\tau | \ln J_z) = \frac{P(\ln J_z | \tau)P(\tau)}{P(\ln J_z)} \quad (3)$$

Because we have taken the step of independently fitting $\lambda(\tau)$ of the calibration sample, the rest of the model parameters described in Section 3.1 (namely, $\mathcal{S}(t_{\ln J_z(\tau)})$ and $\ln V_{\ln J_z}$) must be sufficiently independent from the stellar number density of the calibration sample. Therefore, we take the stellar age prior $P(\tau)$ to be uniform here. Marginalizing over τ allows us to calculate the marginal probability $P(\ln J_z)$:

$$P(\ln J_z) = \int P(\ln J_z | \tau)P(\tau)d\tau \quad (4)$$

In Figure 3, we show a visual illustration of the conditional probabilities $P(\tau | \ln J_z)$ and $P(\ln J_z | \tau)$ in terms of the joint probability $P(\tau, \ln J_z)$. We illustrate using a simulated stellar sample generated from the mean posterior dynamical age model with the stellar number density $\lambda(\tau)$ marginalized out.

To draw the mean posterior dynamical age model in age– $\ln J_z$ space, we first generate a test grid τ_{grid} of possible stellar ages from 0 to 14 Gyr, arbitrarily spaced by 0.014 Gyr. We then evaluate the $\tau(\ln J_z)$ monotonic spline at each point on τ_{grid} using the mean posterior $\mathcal{S}(t_{\tau(\ln J_z)})$ knot values. We take the $\ln J_z$ values on the mean posterior spline corresponding to τ_{grid} to be $\ln J_{z\text{grid}}$. The mean posterior age– $\ln J_z$ splines evaluated over τ_{grid} (in other words, τ_{grid} vs. $\ln J_{z\text{grid}}$) are shown in red in the left panels of Figure 4.

To calculate $P(\tau | \ln J_z)$ for a star of interest with a given $\ln J_z$, we evaluate Equations 3 and 4. We evaluate the integral in Equation 4 numerically with Simpson’s rule across $\ln J_{z\text{grid}}$ to generate a stellar age probability distribution across τ_{grid} . With this, we are able to take any given J_z value and generate a predicted dynamical age probability distribution, evaluated across τ_{grid} .

In Figure 4, we present a comparison of the age– $\ln J_z$ model fit between the RGB calibration sample and MSTO sample. On the left panels, we show both calibration samples in (asteroseismic or isochrone) age vs. J_z space with the best-fit model over-plotted. On the right panels, we show generated age prediction distributions for a set of test

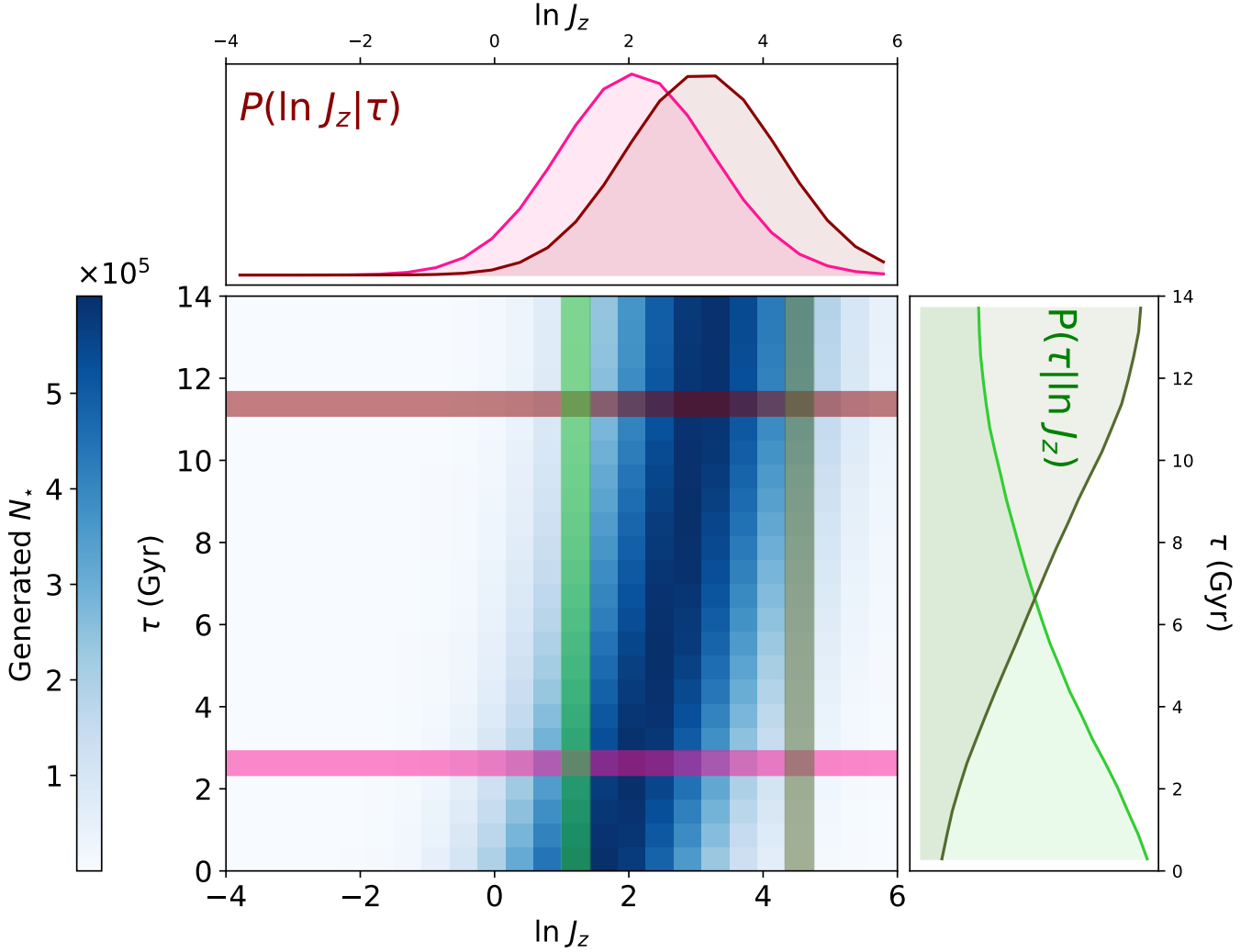


Figure 3. Illustration of the conditional probabilities $P(\ln J_z | \tau)$ and $P(\tau | \ln J_z)$ in relation to the joint probability $P(\tau, \ln J_z)$. The blue heatmap represents the joint probability $P(\tau, \ln J_z)$ and shows a simulated stellar sample in τ - $\ln J_z$ space generated from the mean posterior dynamical age model. The pink and red highlighted horizontal regions correspond to the conditional probability $P(\ln J_z | \tau)$, shown on the top panel as probability density functions in the $\ln J_z$ dimension. The light and dark green highlighted vertical regions correspond to the conditional probability $P(\tau | \ln J_z)$, shown on the right panel as probability density functions in the τ dimension. The $P(\tau | \ln J_z)$ probability density functions are analogous to stellar age predictions based on $\ln J_z$ from *Gaia*.

$\ln J_z$ values for both models. We demonstrate that the analogous test age predictions differ, especially for large J_z , due to the J_z distributions of the calibration sample. However, both models agree in terms of relative age (i.e. when stars are ranked in order of youngest to oldest).

4. VALIDATION

4.1. Internal Model Validation

We internally validate the model using a k -fold cross-validation method. We split each calibration sample randomly into 10 equal subsamples. We designate one subsample as the “withheld” subsample, and the other nine subsamples combined as the “validation” sample. We calibrate the dynamical age model using the validation sample. We then evaluate the calibrated model’s goodness of fit using the withheld subsample, with

$$\chi = \frac{\tau - \tau_{pred}}{\sqrt{V + \sigma_\tau^2}} \quad (5)$$

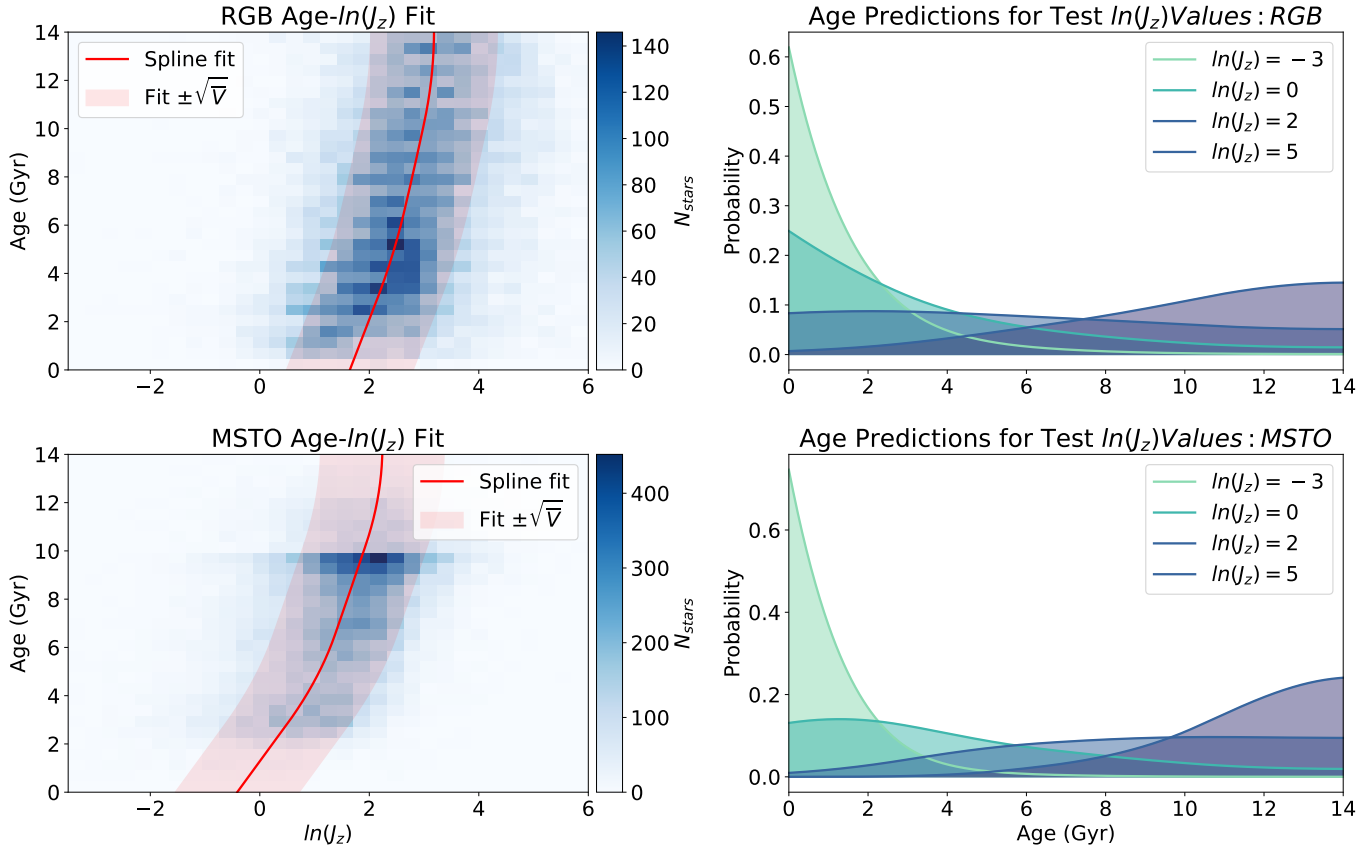


Figure 4. *Top left:* 2-D histogram of the RGB calibration sample in [Stokholm et al. \(2023\)](#) asteroseismic age vs. $\ln J_z$ space. The mean posterior τ - $\ln J_z$ monotonic spline is overplotted, \pm the square root of the best-fit intrinsic variance. *Bottom left:* 2-D histogram of the MSTO calibration sample in [Queiroz et al. \(2023\)](#) isochrone ages vs. $\ln J_z$ space. *Top right:* Generated age prediction distributions for a set of test $\ln J_z$ values using the RGB-calibrated model. *Bottom right:* Generated age prediction distributions for the same set of test $\ln J_z$ values using the MSTO-calibrated model.

where τ represents the stellar ages for the withheld sample, τ_{pred} represents the mean dynamical age predictions for the withheld sample, V is the mean posterior intrinsic variance, and σ_τ represents the stellar age error for the withheld sample. We repeat this process 10 times, where each of the 10 subsamples in turn becomes the withheld sample. We verify that σ_χ (the standard deviation of χ for each of the ten iterations) is close to 1.

We additionally verify that from the calibrated dynamical age model, we are able to reproduce both the age-action trend and the stellar number density of the calibration sample. A visualization of this verification is shown in [Figure 5](#). On the left panel, we show $\ln J_z$ vs. age for the RGB calibration sample as a 2-D histogram with arbitrary bins, along with the best-fit age- J_z model shown in red. The color corresponds to the number density of stars appearing in each bin. On the right panel, we show the number density in each bin predicted by our model. The dynamical age model encodes information about both the age-action trend and the calibration sample number density; however, in predicting ages for stars given $\ln J_z$, we do not consider the number density factor $\lambda(\tau)$.

4.2. Comparison with Asteroseismic RGB Ages

We validate our model-predicted ages against another independent sample of red giant branch stars with asteroseismic age predictions. In [Figure 6](#), we show a column-normalized heatmap of stellar ages from the APOKASC catalog ([Pinsonneault et al. 2018](#)), which derived spectroscopic and asteroseismic ages for red giant stars. The [Pinsonneault et al. \(2018\)](#) sample closely matches the RGB calibration sample in terms of stellar mass and temperature distribution, but have ages determined independently of dynamics. We calculated vertical actions for the stars in the [Pinsonneault et al. \(2018\)](#) sample that have *Gaia* DR3 radial velocities. With [Figure 6](#), we demonstrate that our dynamical age predictions are consistent in age- $\ln J_z$ space with the [Pinsonneault et al. \(2018\)](#) sample, where the $\ln J_z$ distribution is comparable to our calibration sample. The age predictions based on dynamics alone are both truncated and poorly

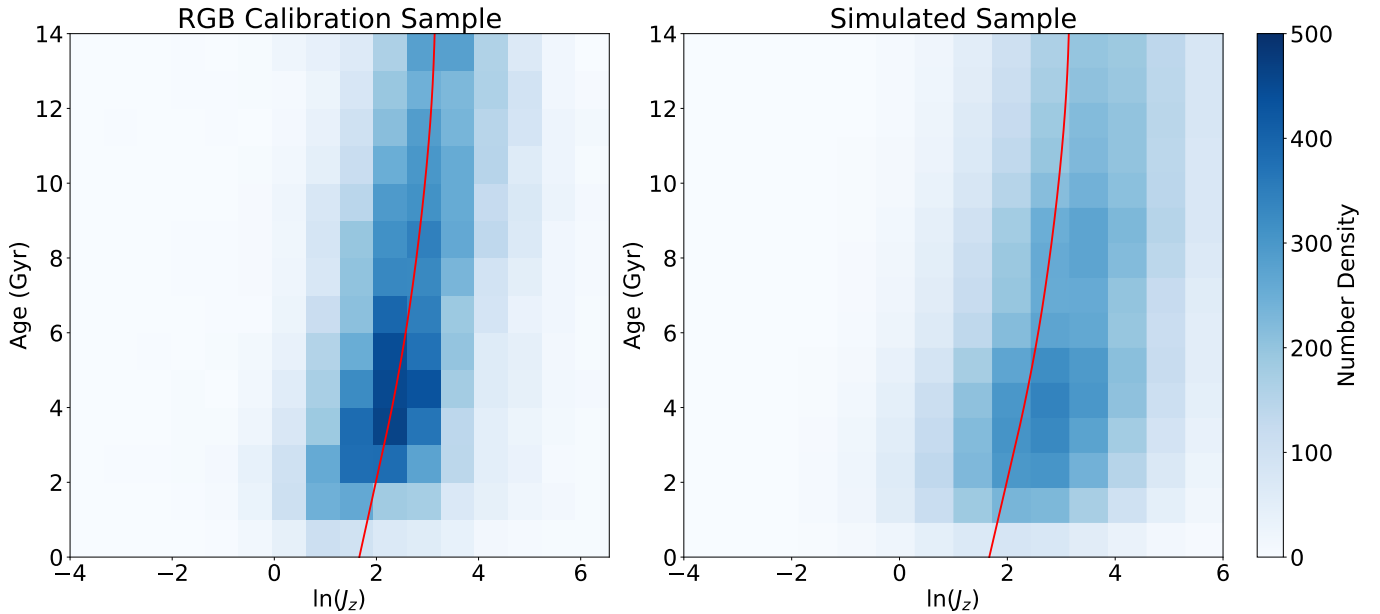


Figure 5. *Left:* 2-D histogram of the red giant calibration sample, and the mean (ridgeline) of the model fit (red). *Right:* Predicted density of stellar ages from model fit (red). While we fit and can re-generate the stellar number density along the age axis according to the calibration sample, we ignore this number density when predicting stellar ages, effectively using only the age- J_z spline model represented in red.

constrained, but we seek to demonstrate that our dynamical age predictions are consistent with independent age measurements.

5. RESULTS

We publish the dynamical age model as an open-source, user-friendly tool called `zoomies`¹ (Sagear & Price-Whelan 2024). This tool takes an input of *Gaia* data for any star with a *Gaia* radial velocity and outputs a predicted age distribution. We use this tool to generate dynamical age predictions for several samples of stars.

We note that dynamical age predictions generated by this tool are dependent on the precision and accuracy of ages in the calibration samples, as seen in the differing age probability distributions given $\ln J_z$ associated with each calibrated model, shown in Figure 4. Indeed, the uncertainty in the age- $\ln J_z$ relation contributes significantly to the wide tails of the age probability distributions (the median age uncertainty for the RGB sample from Stokholm et al. (2023) $\sigma_\tau \approx 1$ Gyr, and for the MSTO sample from Queiroz et al. (2023) $\sigma_\tau \approx 0.5$ Gyr). Age estimates generated for stellar populations that are similar to the calibration sample (in terms of M_\star and $\ln J_z$) may be considered in an absolute sense. However, for stellar populations that differ significantly from the calibration sample, it may be more useful to consider the generated age estimates as relative ages, e.g. in comparing older vs. younger groups within a larger population. We perform a preliminary test to check this assertion, described in Appendix A.

`zoomies` offers functionality for users to calibrate a dynamical age model using any calibration samples with externally measured ages and *Gaia* astrometric data; the precision of the resulting age estimates will depend on the age uncertainties in the chosen calibration sample and the associated scatter along the $\ln J_z$ axis. In the following sections, we compare and discuss our dynamical age estimates for external stellar samples.

5.1. Comparison with Open Cluster ages

We generate dynamical age predictions for open cluster members with independently measured cluster ages. We use the cluster membership lists and ages presented by Dias et al. (2021) to identify individual members of each cluster. We select eight open clusters to present in this paper, and we include an analysis of a random sample of the clusters in Dias et al. (2021) in Appendix D.

¹ www.github.com/ssagear/zoomies

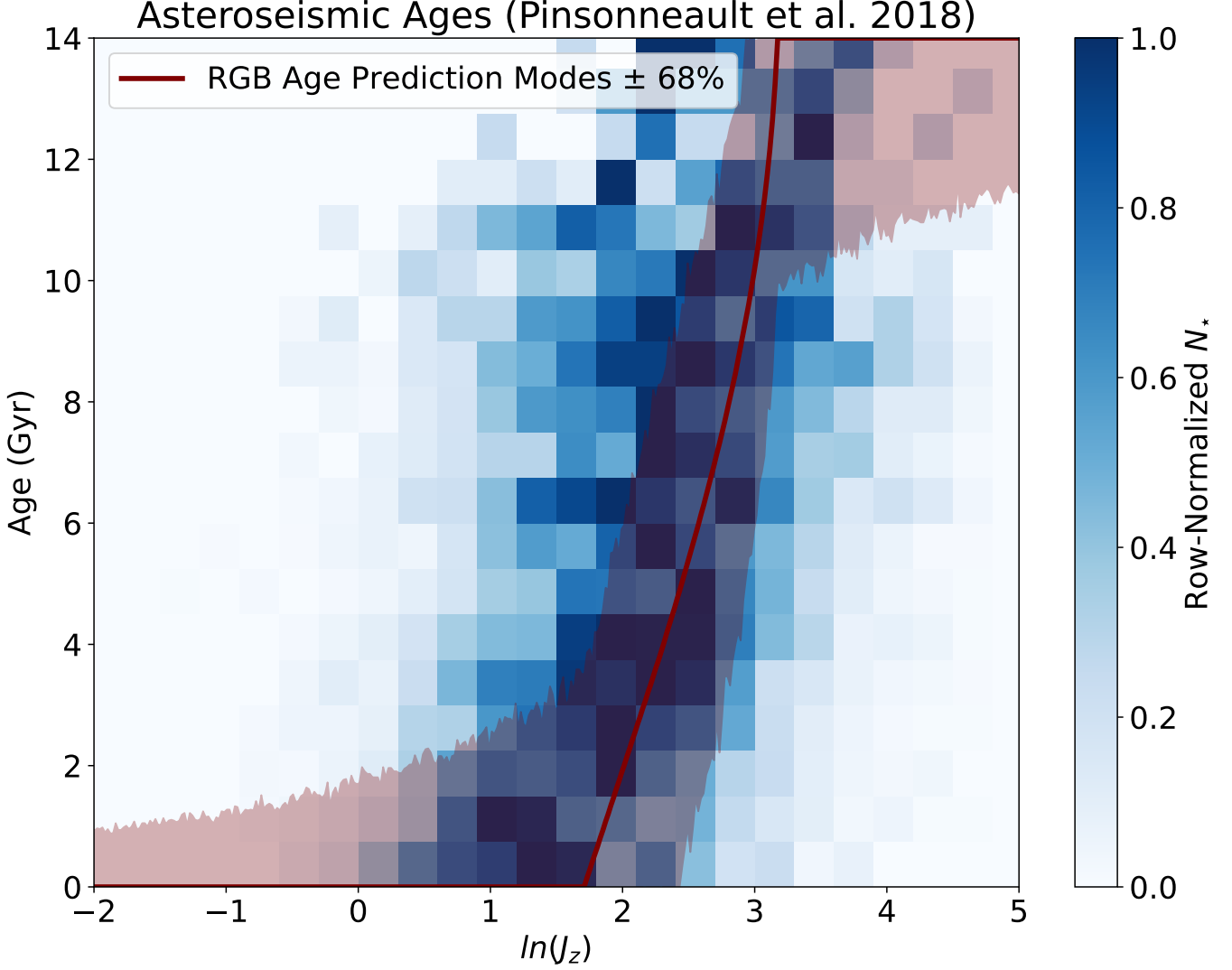


Figure 6. A 2-D histogram of the Pinsonneault et al. (2018) sample of red-giant-branch stars in asteroseismic age- $\ln J_z$ space. The RGB-calibrated dynamical ages for this sample are designated with the red line and shaded region. The solid red line represents the statistical mode of each dynamical age probability distribution associated with each star in the Pinsonneault et al. (2018) sample, and the shaded region represents 68% of the distribution mass around the mode. The 2-D histogram is row-normalized to reduce the visual effect of the stellar density distribution on the τ axis.

We select the eight clusters in Figure 7 with the following method: first, we bin the cluster ages determined by Dias et al. (2021) from 0 to 14 Gyr with an arbitrary width of 1 Gyr. We do this to select an evenly distributed sample of young and old open clusters. Next, we take the cluster in each bin that has the most members, ensuring that each cluster has more than 100 members at this stage. For each cluster, we omit the members that have a membership probability less than 0.5. We consider only the remaining cluster members that have *Gaia* parallaxes > 0 and radial velocities measured. We present the selected clusters, the number of remaining members and their ages in Table 2. We perform the same analysis on a random sample of clusters and include this analysis in Appendix D.

Using the *Gaia* data for this sample, we calculate $\ln J_z$ for each star according to the method described in Section 3. For each cluster, we take the median $\ln J_z$ across all cluster members and generate the corresponding dynamical age probability distribution. We take this age distribution to be the representative age distribution for the entire cluster.

In Figure 7, we show the age distributions for each selected cluster as a violin plot. Though our dynamical age distributions are not as precise as the measured cluster ages, we demonstrate that the relative age predictions for open clusters scale appropriately using only dynamical data.

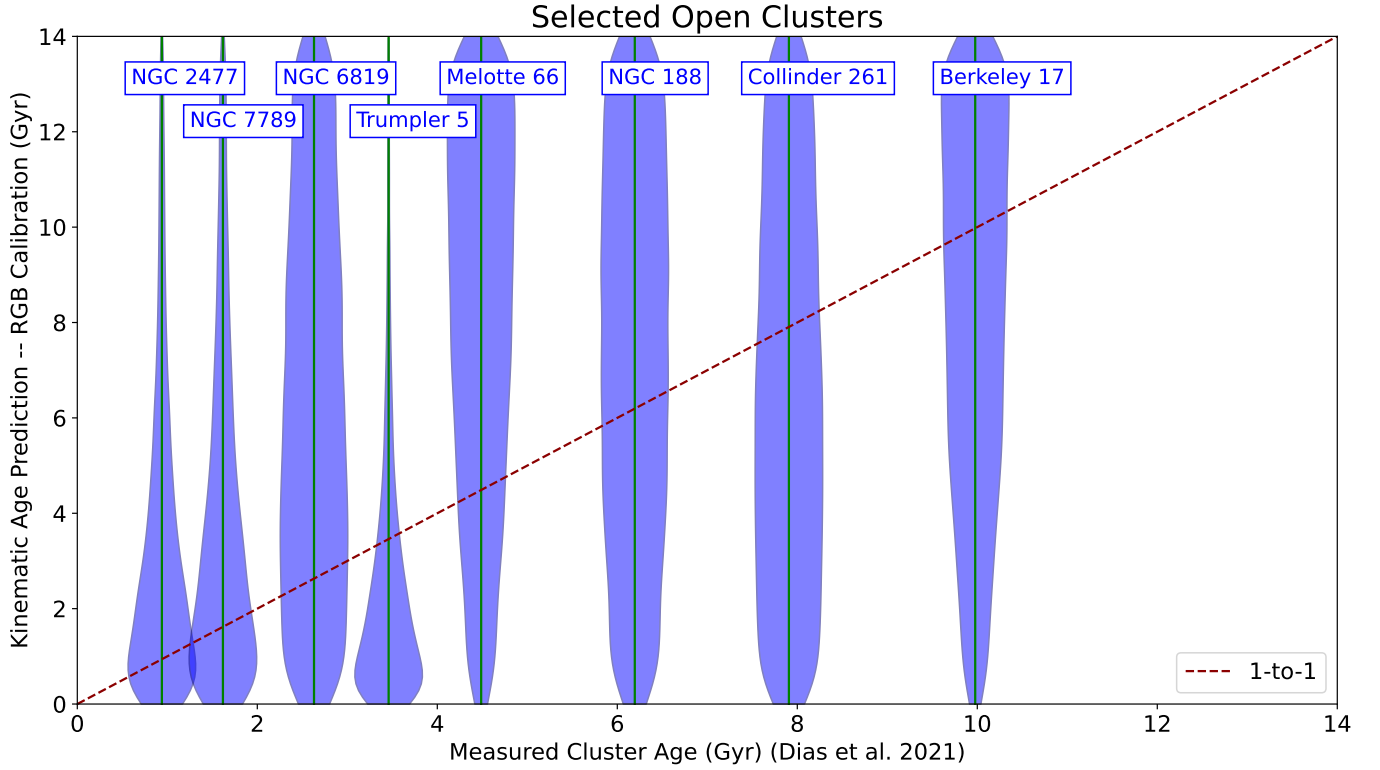


Figure 7. Violin plot of selected open cluster dynamical ages. Each cluster segment is labelled according to the open cluster it represents. Each segment represents the age probability distribution for the median $\ln J_z$ value for cluster members (with arbitrary width), according to the RGB-calibrated dynamical age model. The position of each cluster segment on the x-axis represents the cluster age reported by [Dias et al. \(2021\)](#). The one-to-one relation is shown with the red dotted line. We show that there is broad consistency between the cluster-derived ages and dynamical age predictions, though dynamical age constraints are calibration-limited and much less constraining than the cluster age measurements.

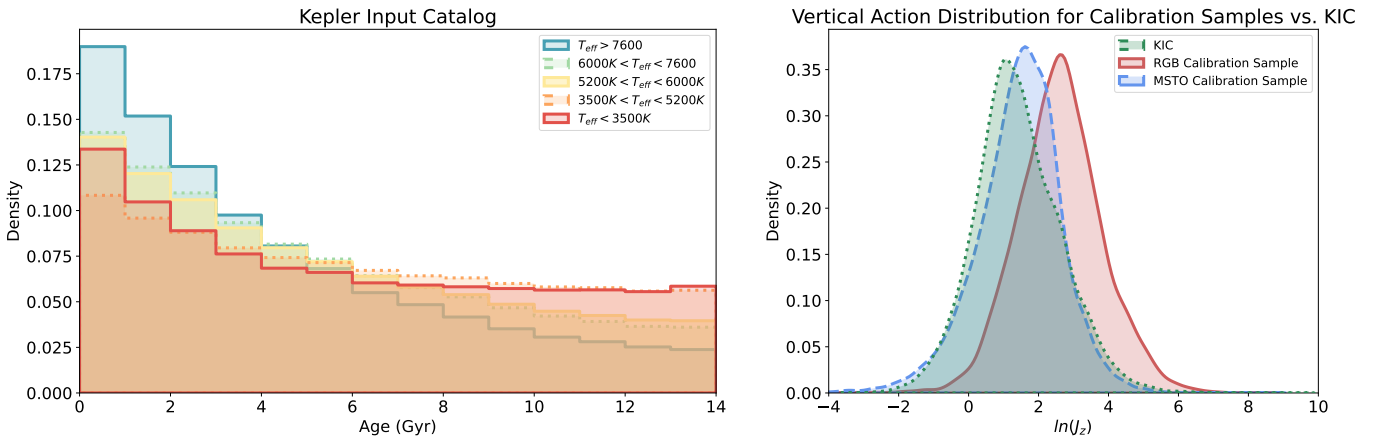


Figure 8. *Left:* Combined dynamical age distributions (calibrated with the MSTO sample) for the KIC sample, partitioned by T_{eff} (from [Mathur et al. 2017](#)). *Right:* $\ln J_z$ distribution for the entire KIC sample (green) compared to the $\ln J_z$ distributions for the RGB and MSTO calibration samples (red and blue, respectively).

5.2. Kepler, K2, and TESS main samples

Table 2. Open cluster sample parameters from [Dias et al. \(2021\)](#). N is the number of cluster members used in analysis after vetting based on availability of *Gaia* parallax and radial velocity, and membership probability ≥ 0.5 according to [Dias et al. \(2021\)](#). $\tau_{Cluster}$ is the independently measured cluster age from [Dias et al. \(2021\)](#).

Cluster	N	$\tau_{Cluster}$ (Gyr)
NGC 2477	421	0.94
NGC 7789	639	1.62
NGC 6819	132	2.63
Trumpler 5	192	3.46
Melotte 66	69	4.49
NGC 188	84	6.19
Collinder 261	105	7.90
Berkeley 17	25	9.98

In this Section, we investigate dynamical ages derived with `zoomies` for several samples of stars from large exoplanet transit surveys. We employ the *Kepler* Input Catalog (KIC) ([Brown et al. 2011](#)) together with the *Gaia-Kepler* cross-match² to identify sources with a *Gaia* radial velocity measurement. We generate dynamical age predictions according to the methods described in Section 3 for 100,885 *Kepler* stars for which we can measure a vertical action. Figure 8 shows combined histograms for *Kepler* stellar age predictions, binned by T_{eff} . For the *Kepler* stellar sample, we have employed the T_{eff} values presented in the *Kepler* Data Release 25 (DR25) catalog ([Mathur et al. 2017](#)). We obtain the data set from the NASA Exoplanet Archive ([Kepler Mission 2019](#))³. We first draw a randomly-chosen 100 points from the stellar age probability distribution generated by `zoomies` for each star, before combining these probability samples for all stars within a given T_{eff} range. As we expect, we find that the hottest stars are more likely to have younger predicted ages, while age predictions for the coolest stars are more uniformly distributed between young and old. We note that the majority of the *Kepler* stellar samples does not match the mass range of our calibration samples, and so emphasize that these age predictions should be carefully considered as relative age predictions rather than absolute ages.

We also present a preliminary comparison of our age predictions with the [Mathur et al. \(2023\)](#) sample of *Kepler* gyrochronological ages. [Mathur et al. \(2023\)](#) measured gyrochronological ages for around 55,000 main-sequence stars using *Kepler*. In Figure 9, we show a comparison of the gyrochronological ages from [Mathur et al. \(2023\)](#) with the analogous dynamical age estimates from the MSTO-calibrated model. We consider the MSTO-calibrated age predictions for the *Kepler* sample because the *Kepler* sample $\ln J_z$ distribution matches the $\ln J_z$ distribution of the MSTO sample more closely than the RGB sample (see Figure 8, right panel).

While the scatter is large for $\tau > 4$ Gyr in age-action space, the positive relationship between $\ln J_z$ and age can be seen for young ages in Figure 9. As we expect, the slope of the dynamical age relation is broadly consistent with the slope seen in age-action space for the [Mathur et al. \(2023\)](#) *Kepler* gyrochronology sample. With this comparison, we demonstrate that dynamical ages generated with this method are consistent with independently measured gyrochronological ages of main-sequence *Kepler* stars primarily for $\tau < 4$ Gyr.

² <https://gaia-kepler.fun/>

³ Accessed on 2023-12-05

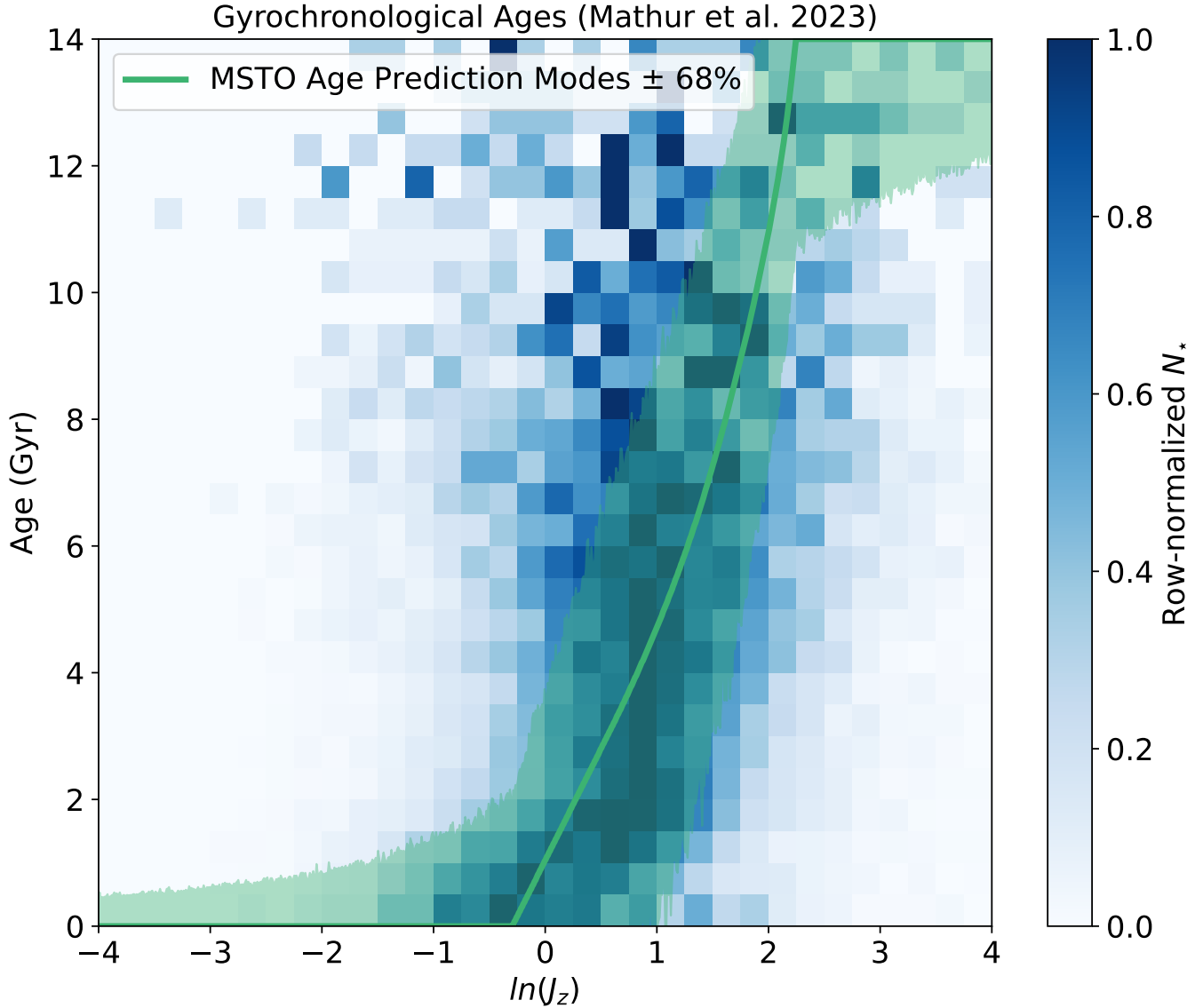


Figure 9. A 2-D histogram of the Mathur et al. (2023) sample of *Kepler* main-sequence stars in gyrochronological age- $\ln J_z$ space. The MSTO-calibrated dynamical ages for this sample are designated with the green line and shaded region. The solid green line represents the statistical mode of each dynamical age probability distribution associated with each star in the Mathur et al. (2023) sample, and the shaded region represents 68% of the distribution mass around the mode. The 2-D histogram is row-normalized to reduce the visual effect of the stellar density distribution on the τ axis.

We compare the ages of the *Kepler*, K2 and *TESS* survey samples. We repeat the process of generating dynamical age estimates for the K2 and *TESS* target stars with positive parallax measurements and radial velocities from *Gaia*. For a consistent comparison, we compare stellar ages within the same selected ranges of T_{eff} . For the K2 stellar sample, we employ the T_{eff} values presented in the K2 Ecliptic Plane Input Catalog (Huber et al. 2016), and for the *TESS* stellar sample, we employ the T_{eff} values presented in the *TESS* Input Catalog 8 (TIC 8) (Stassun et al. 2019). We present the combined age distributions for each survey sample, along with the vertical action distributions, in Figure 10 for two selected temperature ranges. K2 stars appear slightly older on average than *Kepler* stars. Differences in the age distributions between the transit survey samples originate from different mission designs: the surveys’ different selection functions, combined with different pointing strategies, contribute to differences in the average observed stellar populations’ kinematics. While the original *Kepler* mission’s field of view was a small stationary area pointing near, but not directly on, the Galactic plane (Gilliland et al. 2011), the K2 mission observed several target fields along

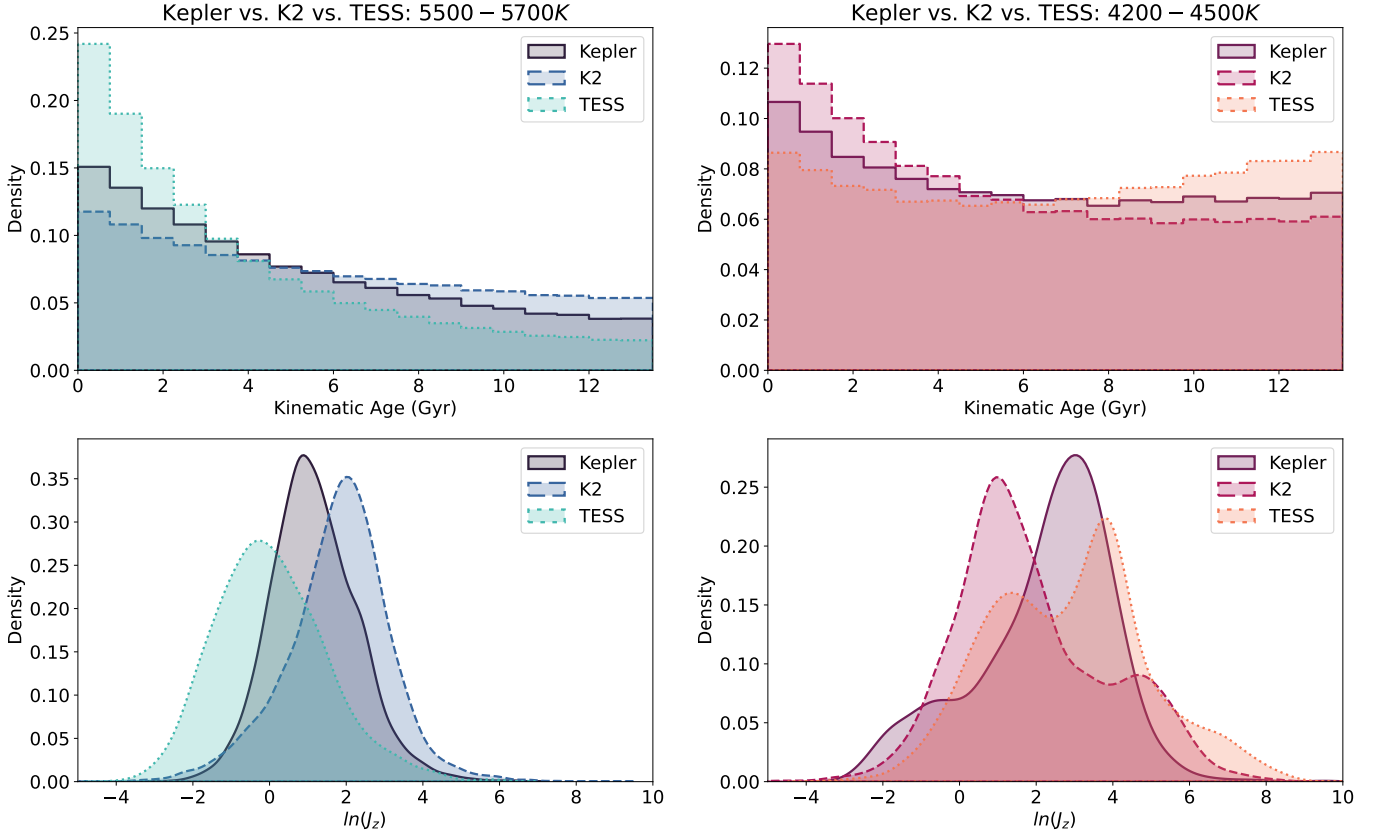


Figure 10. *Top Left:* Combined dynamical age probability distributions for *Kepler* (solid), *K2* (dashed), and *TESS* (dotted) stellar samples with T_{eff} between 5500 and 5700 K. Bin widths arbitrarily set to 0.5 Gyr. *Top Right:* Same as top left, but for stars with T_{eff} between 4200 and 4500 K. *Bottom Left:* Combined $\ln J_z$ kernel density estimations (KDEs) for the *Kepler*, *K2* and *TESS* stars with T_{eff} between 5500 and 5700 K. *Bottom right:* Same as bottom left, but for stars with T_{eff} between 4200 and 4500 K.

the ecliptic across a period of several years (Howell et al. 2014). Yet, both missions use the same instrument and bandpass. This may cause different distributions in vertical action, as seen in Figure 10. In contrast, *TESS*’s wide, near-infrared bandpass and its pointing throughout the celestial sphere (Ricker et al. 2014) may be reflected in the difference in age and vertical action distributions between hotter and cooler *TESS* stars, compared to the *Kepler* and *K2* samples. We have confined ourselves in this manuscript to a description of the *zoomies* machinery, and leave its detailed application to exoplanetary studies to future work. However, we comment upon large-scale trends to emphasize the potential usefulness of dynamical ages to the exoplanet community.

6. DISCUSSION

In the following subsections, we return to our assumptions about the dynamical age model’s dependence on stellar mass and discuss the limitations of our model related to sample distributions in action space. We also discuss the implications of these results on planet occurrence.

6.1. Stellar Mass Dependence

As discussed in Section 1 and Section 3, we assume in our dynamical age relation that the kinematic galactic motion of stars are mass-independent, consistent with an “upside-down” and “inside-out” model of galactic assembly (Bird et al. 2013, 2021). Alternatively, it is possible that the AVR is driven primarily by orbital heating (e.g. Spitzer & Schwarzschild 1953). If stellar kinematic properties are determined primarily by orbital heating, the dynamical age model we construct will not be entirely mass-independent and may produce less accurate age predictions for stars with masses significantly different from our calibration sample (i.e. the lowest-mass stars). However, we contend that in this case, this dynamical age relation is still far less dependent on stellar mass than other age determination methods, such

as isochrone fitting and asteroseismic ages, especially when interpreting age predictions as relative ages for low-mass stars. In order to avoid any mass dependence in a dynamical age model, a large calibration sample of low-mass stars with relatively confident age measurements is needed.

6.2. Impact of the full orbital action distribution on age predictions

Here we discuss the extent to which one may apply the dynamical age model to prediction samples that do not closely match the calibration sample in action space. In selecting a calibration sample, we necessarily assume that the $\ln J_z$ distribution of the calibration sample matches that of the prediction sample of interest. However, we selected the RGB and MSTO samples primarily because of the accuracy and precision of their ages determined with asteroseismology and isochrone-fitting, respectively (not necessarily because their $\ln J_z$ distributions match the $\ln J_z$ distributions of our prediction samples). In many cases, sufficiently large calibration samples with accurate, independently-measured ages that also match the $\ln J_z$ distribution of the prediction sample are not available. This is particularly likely for the lowest-mass stars, which also happen to be the most prominent exoplanet hosts.

We calibrate the dynamical age model in this work on J_z , which represents one slice of a three dimensional projection of action space, including J_z , J_r , and J_ϕ . We contend that the best way to mitigate the effects of prediction sample that do not match the calibration sample is to build a joint age–action model that considers all three actions. We will address this in a future work, as an age prediction method based on all orbital actions should produce more precise ages. However, short of building a three-dimensional age–action model, one workaround with the current one-dimensional method is to re-sample or re-weight the prediction sample in action space to more closely match the calibration sample.

6.3. Planet Occurrence and Dynamical Ages

The investigation of planet formation and evolution is only one application of demographic stellar age constraints. While we aim for *zoomies* to be broadly useful the astronomical community interested in stellar ages in the Milky Way, we focus here on its potential use for studying exoplanet host stars. *Gaia* has enabled exoplanet study to occur within a new Galactic context (see e.g. Winter et al. 2020; Dai et al. 2021; Chen et al. 2021a; Longmore et al. 2021; Bashi & Zucker 2021; Zink et al. 2023). In this Section, we describe the relative strength of dynamically-derived stellar ages for investigations of the (on average) $\mathcal{O}10^5 - 10^6$ stars monitored by space-based transit surveys.

Folding together both isochrone or spectroscopic age constraints together with *Gaia* parallaxes or kinematic measurements, the evolution of planetary systems over time has already been seen (Berger et al. 2023; Chen et al. 2021b). For example, the radius distribution of planets shifts as stars age (Berger et al. 2020b), and there exists an apparent change in transit multiplicity as well (Chen et al. 2021b). Zink et al. (2023) found that raw occurrence is affected by Galactic height (as determined by *Gaia* parallaxes), one of many proxies for stellar age. We consider the dynamical ages for the population of stars observed by *Kepler*. Nominally, we might expect to see some trend with age– though dynamical age dating involves much larger uncertainty than other methods.

The degree to which the dynamical age relation we developed is constraining at the population level for the *Kepler* sample is shown in Figure 11. We overplot the dynamical age distributions for the entire sample of *Kepler* Objects of Interest (KOI), versus KIC field stars with no transiting planets. We do see a visible offset in the same direction as Chen et al. (2021b): that is, host stars to transiting planets are, on average, younger than field stars. This figure is meant to convey the relative strength of dynamical age information alone: fully disambiguating the ages of field stars vs. planet hosts would require many additional steps (given that the population of field stars in fact hosts planets too, though not in a transiting geometry). In this sense, the KIC sample is contaminated with planet hosts and not representative of stars that don’t have planets. Even given this degree of contamination, Figure 11 shows to first order the extent to which dynamical information alone can be useful at a demographic level.

7. CONCLUSIONS

We summarize our results and work as follows:

- We calibrate a flexible model to predict stellar ages given the vertical actions of stars using two independent calibration samples: one based on asteroseismic red giant branch star ages and one using isochrone main-sequence turn-off star ages.
- We compare these dynamical age predictions with an external sample of red giant branch stars with asteroseismic and spectroscopic ages and find general agreement, though our age predictions are less precise (as expected).

Combined Ages: KOIs vs. KICs

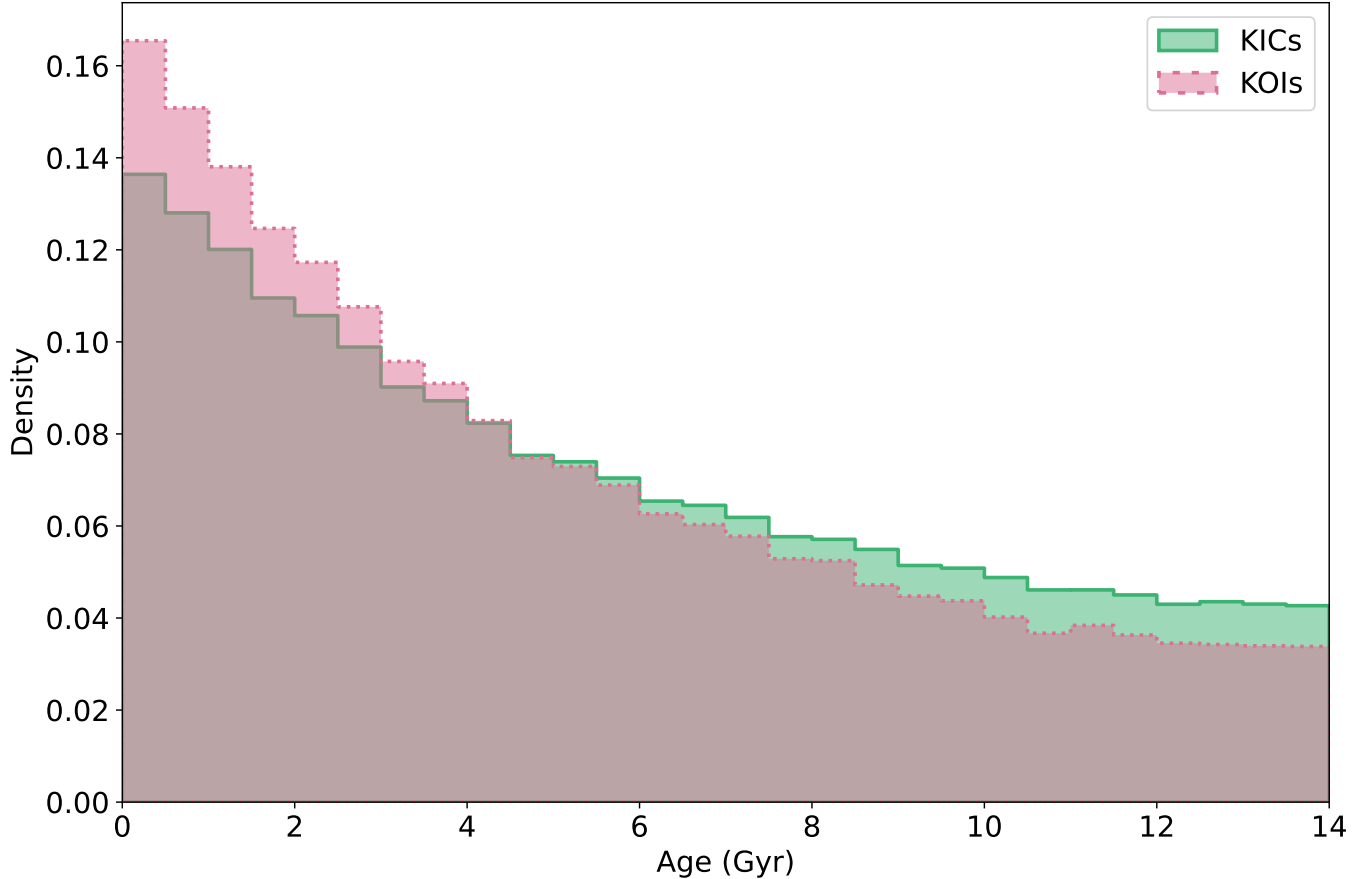


Figure 11. Combined dynamical age distributions for the entire KIC catalog (green) and all KOIs (red).

- We compare our dynamical age predictions with measured ages for open clusters and main-sequence stars with gyrochronological ages and again find that our ages agree with other independent methods, at least in relative age ranking.
- We produce age predictions for the *Kepler*, K2, and *TESS* main samples and show that the stars observed by these surveys have naturally different Galactic kinematics and intrinsic age distributions.
- We release our model and the age prediction tools used in this analysis in an open-source, user-friendly software package called **zoomies** (Sagear & Price-Whelan 2024).

The magnitude and precision of *Gaia* data that have become available in recent years allows us to generate homogeneous, mass-independent relative age predictions using only astrometric data and a potential model of the Milky Way. This newly enables large-scale age analyses on a wide range of stellar masses, even the lowest-mass stars. These dynamical ages can be useful for any investigation involving stellar populations, and especially for demographic studies of the lowest-mass exoplanet hosts and the dynamical evolution of their planetary systems. In a future work, we plan to combine orbital eccentricity information for planet-hosting stars (e.g. Van Eylen et al. 2019; Sagear & Ballard 2023) with homogeneous stellar metallicity information (e.g. Anderson et al. 2021) to disentangle the underlying relationship between planet occurrence, orbital dynamics, metallicity, and age.

We thank the anonymous referees for helpful suggestions that improved the quality of this work. We thank Jamie Tayar and Zachary Claytor for careful readings of this manuscript, along with Christopher Lam, Quadry Chance, Natalia Guerrero, Dana Yaptangco, Nazar Budaiev, and Soichiro Hattori for helpful discussions about this analysis.

This work has made use of data from the European Space Agency (ESA) mission *Gaia* (<https://www.cosmos.esa.int/gaia>), processed by the *Gaia* Data Processing and Analysis Consortium (DPAC, <https://www.cosmos.esa.int/web/>

[gaia/dpac/consortium](#)). Funding for the DPAC has been provided by national institutions, in particular the institutions participating in the *Gaia* Multilateral Agreement. This paper includes data collected by the Kepler, K2, and TESS missions and obtained from the MAST data archive at the Space Telescope Science Institute (STScI). The specific observations analyzed can be accessed via <https://doi.org/10.17909/T9059R> (KIC), <https://doi.org/10.17909/T93W28> (EPIC), and <https://doi.org/10.17909/fwdt-2x66> (TIC). STScI is operated by the Association of Universities for Research in Astronomy, Inc., under NASA contract NAS5–26555. Support to MAST for these data is provided by the NASA Office of Space Science via grant NAG5–7584 and by other grants and contracts. This research has made use of the NASA Exoplanet Archive, which is operated by the California Institute of Technology, under contract with the National Aeronautics and Space Administration under the Exoplanet Exploration Program.

Facilities: Gaia, Kepler, TESS, Exoplanet Archive, MAST

Software: numpy (Harris et al. 2020), matplotlib (Caswell et al. 2024), astropy (Robitaille et al. 2013; Collaboration et al. 2018, 2022), numpyro (Bingham et al. 2019; Phan et al. 2019), gala (Price-Whelan 2017; Price-Whelan et al. 2020), agama (Vasiliev 2019)

REFERENCES

- Almeida-Fernandes, F., & Rocha-Pinto, H. J. 2018, Monthly Notices of the Royal Astronomical Society, 476, 184, doi: [10.1093/mnras/sty119](https://doi.org/10.1093/mnras/sty119)
- Anderson, S. G., Dittmann, J. A., Ballard, S., & Bedell, M. 2021, The Astronomical Journal, 161, 203, doi: [10.3847/1538-3881/abe70b](https://doi.org/10.3847/1538-3881/abe70b)
- Angus, R., Beane, A., Price-Whelan, A. M., et al. 2020, The Astronomical Journal, 160, 90, doi: [10.3847/1538-3881/ab91b2](https://doi.org/10.3847/1538-3881/ab91b2)
- Aumer, M., Binney, J., & Schönrich, R. 2016, Monthly Notices of the Royal Astronomical Society, 462, 1697, doi: [10.1093/mnras/stw1639](https://doi.org/10.1093/mnras/stw1639)
- Barnes, S. A. 2007, The Astrophysical Journal, 669, 1167, doi: [10.1086/519295](https://doi.org/10.1086/519295)
- Bashi, D., & Zucker, S. 2021, Astronomy & Astrophysics, 651, A61, doi: [10.1051/0004-6361/202140699](https://doi.org/10.1051/0004-6361/202140699)
- Berger, T. A., Huber, D., Gaidos, E., van Saders, J. L., & Weiss, L. M. 2020a, The Astronomical Journal, 160, 108, doi: [10.3847/1538-3881/aba18a](https://doi.org/10.3847/1538-3881/aba18a)
- Berger, T. A., Huber, D., van Saders, J. L., et al. 2020b, The Astronomical Journal, 159, 280, doi: [10.3847/1538-3881/159/6/280](https://doi.org/10.3847/1538-3881/159/6/280)
- Berger, T. A., Schlieder, J. E., & Huber, D. 2023, The Gaia-Kepler-TESS-Host Stellar Properties Catalog: Uniform Physical Parameters for 7993 Host Stars and 9324 Planets, arXiv. <http://arxiv.org/abs/2301.11338>
- Bingham, E., Chen, J. P., Jankowiak, M., et al. 2019, Journal of Machine Learning Research, 20, 1. <http://jmlr.org/papers/v20/18-403.html>
- Bird, J. C., Kazantzidis, S., Weinberg, D. H., et al. 2013, The Astrophysical Journal, 773, 43, doi: [10.1088/0004-637X/773/1/43](https://doi.org/10.1088/0004-637X/773/1/43)
- Bird, J. C., Loebman, S. R., Weinberg, D. H., et al. 2021, Monthly Notices of the Royal Astronomical Society, 503, 1815, doi: [10.1093/mnras/stab289](https://doi.org/10.1093/mnras/stab289)
- Borucki, W. J., Koch, D., Basri, G., et al. 2010, Science, 327, 977, doi: [10.1126/science.1185402](https://doi.org/10.1126/science.1185402)
- Boyajian, T. S., Braun, K. v., Belle, G. v., et al. 2012, The Astrophysical Journal, 757, 112, doi: [10.1088/0004-637X/757/2/112](https://doi.org/10.1088/0004-637X/757/2/112)
- Brown, T. M., Latham, D. W., Everett, M. E., & Esquerdo, G. A. 2011, The Astronomical Journal, 142, 112, doi: [10.1088/0004-6256/142/4/112](https://doi.org/10.1088/0004-6256/142/4/112)
- Cai, M. X., Kouwenhoven, M. B. N., Portegies Zwart, S. F., & Spurzem, R. 2017, Monthly Notices of the Royal Astronomical Society, 470, 4337, doi: [10.1093/mnras/stx1464](https://doi.org/10.1093/mnras/stx1464)
- Caswell, T. A., Andrade, E. S. d., Lee, A., et al. 2024, matplotlib/matplotlib: REL: v3.7.5, Zenodo, doi: [10.5281/zenodo.10669804](https://doi.org/10.5281/zenodo.10669804)
- Chen, D.-C., Yang, J.-Y., Xie, J.-W., et al. 2021a, The Astronomical Journal, 162, 100, doi: [10.3847/1538-3881/ac0f08](https://doi.org/10.3847/1538-3881/ac0f08)
- Chen, D.-C., Xie, J.-W., Zhou, J.-L., et al. 2021b, The Astrophysical Journal, 909, 115, doi: [10.3847/1538-4357/abd5be](https://doi.org/10.3847/1538-4357/abd5be)
- Choi, J., Dotter, A., Conroy, C., et al. 2016, The Astrophysical Journal, 823, 102, doi: [10.3847/0004-637X/823/2/102](https://doi.org/10.3847/0004-637X/823/2/102)
- Collaboration, T. A., Price-Whelan, A. M., Sipőcz, B. M., et al. 2018, The Astronomical Journal, 156, 123, doi: [10.3847/1538-3881/aabc4f](https://doi.org/10.3847/1538-3881/aabc4f)
- Collaboration, T. A., Price-Whelan, A. M., Lim, P. L., et al. 2022, The Astrophysical Journal, 935, 167, doi: [10.3847/1538-4357/ac7c74](https://doi.org/10.3847/1538-4357/ac7c74)

- Cui, X.-Q., Zhao, Y.-H., Chu, Y.-Q., et al. 2012, *Research in Astronomy and Astrophysics*, 12, 1197, doi: [10.1088/1674-4527/12/9/003](https://doi.org/10.1088/1674-4527/12/9/003)
- Dai, Y.-Z., Liu, H.-G., An, D.-S., & Zhou, J.-L. 2021, *The Astronomical Journal*, 162, 46, doi: [10.3847/1538-3881/ac00ad](https://doi.org/10.3847/1538-3881/ac00ad)
- Darragh-Ford, E., Mantz, A. B., Rasia, E., et al. 2023, *Monthly Notices of the Royal Astronomical Society*, 521, 790, doi: [10.1093/mnras/stad585](https://doi.org/10.1093/mnras/stad585)
- De Silva, G. M., Freeman, K. C., Bland-Hawthorn, J., et al. 2015, *Monthly Notices of the Royal Astronomical Society*, 449, 2604, doi: [10.1093/mnras/stv327](https://doi.org/10.1093/mnras/stv327)
- Dias, W. S., Monteiro, H., Moitinho, A., et al. 2021, *Monthly Notices of the Royal Astronomical Society*, 504, 356, doi: [10.1093/mnras/stab770](https://doi.org/10.1093/mnras/stab770)
- Eilers, A.-C., Hogg, D. W., Rix, H.-W., & Ness, M. K. 2019, *The Astrophysical Journal*, 871, 120, doi: [10.3847/1538-4357/aaf648](https://doi.org/10.3847/1538-4357/aaf648)
- Epstein, C. R., & Pinsonneault, M. H. 2013, *The Astrophysical Journal*, 780, 159, doi: [10.1088/0004-637X/780/2/159](https://doi.org/10.1088/0004-637X/780/2/159)
- Everall, A., & Das, P. 2020, *Monthly Notices of the Royal Astronomical Society*, 493, 2042, doi: [10.1093/mnras/staa283](https://doi.org/10.1093/mnras/staa283)
- Everall, A., Evans, N. W., Belokurov, V., Boubert, D., & Grand, R. J. J. 2022, *Monthly Notices of the Royal Astronomical Society*, 511, 2390, doi: [10.1093/mnras/stab3325](https://doi.org/10.1093/mnras/stab3325)
- Faherty, J. K., Burgasser, A. J., Cruz, K. L., et al. 2009, *The Astronomical Journal*, 137, 1, doi: [10.1088/0004-6256/137/1/1](https://doi.org/10.1088/0004-6256/137/1/1)
- Feiden, G. A., & Chaboyer, B. 2012, *The Astrophysical Journal*, 757, 42, doi: [10.1088/0004-637X/757/1/42](https://doi.org/10.1088/0004-637X/757/1/42)
- Fulton, B. J., & Petigura, E. A. 2018, *The Astronomical Journal*, 156, 264, doi: [10.3847/1538-3881/aae828](https://doi.org/10.3847/1538-3881/aae828)
- Gelman, A., & Rubin, D. B. 1992, *Statistical Science*, 7, 457, doi: [10.1214/ss/1177011136](https://doi.org/10.1214/ss/1177011136)
- Gilliland, R. L., Chaplin, W. J., Dunham, E. W., et al. 2011, *The Astrophysical Journal Supplement Series*, 197, 6, doi: [10.1088/0067-0049/197/1/6](https://doi.org/10.1088/0067-0049/197/1/6)
- Grand, R. J. J., Springel, V., Gómez, F. A., et al. 2016, *Monthly Notices of the Royal Astronomical Society*, 459, 199, doi: [10.1093/mnras/stw601](https://doi.org/10.1093/mnras/stw601)
- Guerrero, N. M., Seager, S., Huang, C. X., et al. 2021, *The Astrophysical Journal Supplement Series*, 254, 39, doi: [10.3847/1538-4365/abefel](https://doi.org/10.3847/1538-4365/abefel)
- Harris, C. R., Millman, K. J., van der Walt, S. J., et al. 2020, *Nature*, 585, 357, doi: [10.1038/s41586-020-2649-2](https://doi.org/10.1038/s41586-020-2649-2)
- Holmberg, J., Nordström, B., & Andersen, J. 2007, *Astronomy & Astrophysics*, 475, 519, doi: [10.1051/0004-6361:20077221](https://doi.org/10.1051/0004-6361:20077221)
- Homan, M. D., & Gelman, A. 2014, *The Journal of Machine Learning Research*, 15, 1593
- House, E. L., Brook, C. B., Gibson, B. K., et al. 2011, *Monthly Notices of the Royal Astronomical Society*, 415, 2652, doi: [10.1111/j.1365-2966.2011.18891.x](https://doi.org/10.1111/j.1365-2966.2011.18891.x)
- Howell, S. B., Sobek, C., Haas, M., et al. 2014, *Publications of the Astronomical Society of the Pacific*, 126, 398, doi: [10.1086/676406](https://doi.org/10.1086/676406)
- Huber, D., Chaplin, W. J., Christensen-Dalsgaard, J., et al. 2013, *The Astrophysical Journal*, 767, 127, doi: [10.1088/0004-637X/767/2/127](https://doi.org/10.1088/0004-637X/767/2/127)
- Huber, D., Bryson, S. T., Haas, M. R., et al. 2016, *The Astrophysical Journal Supplement Series*, 224, 2, doi: [10.3847/0067-0049/224/1/2](https://doi.org/10.3847/0067-0049/224/1/2)
- Hänninen, J., & Flynn, C. 2002, *Monthly Notices of the Royal Astronomical Society*, 337, 731, doi: [10.1046/j.1365-8711.2002.05956.x](https://doi.org/10.1046/j.1365-8711.2002.05956.x)
- Karataş, Y., Bilir, S., & Schuster, W. J. 2005, *Monthly Notices of the Royal Astronomical Society*, 360, 1345, doi: [10.1111/j.1365-2966.2005.09120.x](https://doi.org/10.1111/j.1365-2966.2005.09120.x)
- Kepler Mission. 2019, *Kepler Stellar Properties Table*, [object Object], doi: [10.26133/NEA6](https://doi.org/10.26133/NEA6)
- Kiman, R., Schmidt, S. J., Angus, R., et al. 2019, *The Astronomical Journal*, 157, 231, doi: [10.3847/1538-3881/ab1753](https://doi.org/10.3847/1538-3881/ab1753)
- Lebreton, Y., & Montalbán, J. 2009, *IAU Symp.*, 258, 419, doi: [10.1017/S1743921309032074](https://doi.org/10.1017/S1743921309032074)
- Lombardi, M., Lada, C. J., & Alves, J. 2013, *Astronomy & Astrophysics*, 559, A90, doi: [10.1051/0004-6361/201321827](https://doi.org/10.1051/0004-6361/201321827)
- Longmore, S. N., Chevance, M., & Kruijssen, J. M. D. 2021, *The Astrophysical Journal Letters*, 911, L16, doi: [10.3847/2041-8213/abeb22](https://doi.org/10.3847/2041-8213/abeb22)
- Lu, Y., Angus, R., Foreman-Mackey, D., & Hattori, S. 2024a, *The Astronomical Journal*, 167, 159, doi: [10.3847/1538-3881/ad28b9](https://doi.org/10.3847/1538-3881/ad28b9)
- Lu, Y. L., Angus, R., Curtis, J. L., David, T. J., & Kiman, R. 2021, *The Astronomical Journal*, 161, 189, doi: [10.3847/1538-3881/abe4d6](https://doi.org/10.3847/1538-3881/abe4d6)
- Lu, Y. L., See, V., Amard, L., Angus, R., & Matt, S. P. 2024b, *Nature Astronomy*, 8, 223, doi: [10.1038/s41550-023-02126-2](https://doi.org/10.1038/s41550-023-02126-2)
- Majewski, S. R., Schiavon, R. P., Frinchaboy, P. M., et al. 2017, *The Astronomical Journal*, 154, 94, doi: [10.3847/1538-3881/aa784d](https://doi.org/10.3847/1538-3881/aa784d)

- Mann, A. W., Dupuy, T., Kraus, A. L., et al. 2019, *The Astrophysical Journal*, 871, 63, doi: [10.3847/1538-4357/aaf3bc](https://doi.org/10.3847/1538-4357/aaf3bc)
- Martell, S. L., Sharma, S., Buder, S., et al. 2017, *Monthly Notices of the Royal Astronomical Society*, 465, 3203, doi: [10.1093/mnras/stw2835](https://doi.org/10.1093/mnras/stw2835)
- Mathur, S., Huber, D., Batalha, N. M., et al. 2017, *The Astrophysical Journal Supplement Series*, 229, 30, doi: [10.3847/1538-4365/229/2/30](https://doi.org/10.3847/1538-4365/229/2/30)
- Mathur, S., Claytor, Z. R., Santos, A. R. G., et al. 2023, *The Astrophysical Journal*, 952, 131, doi: [10.3847/1538-4357/acd118](https://doi.org/10.3847/1538-4357/acd118)
- McCluskey, F., Wetzel, A., Loebman, S. R., et al. 2024, *Monthly Notices of the Royal Astronomical Society*, 527, 6926, doi: [10.1093/mnras/stad3547](https://doi.org/10.1093/mnras/stad3547)
- Mints, A., & Hekker, S. 2017, *Astronomy & Astrophysics*, 604, A108, doi: [10.1051/0004-6361/201630090](https://doi.org/10.1051/0004-6361/201630090)
- . 2018, *Astronomy & Astrophysics*, 618, A54, doi: [10.1051/0004-6361/201832739](https://doi.org/10.1051/0004-6361/201832739)
- Miyamoto, M., & Nagai, R. 1975, *Publications of the Astronomical Society of Japan*, 27, 533. <https://ui.adsabs.harvard.edu/abs/1975PASJ...27..533M>
- Mulders, G. D., Pascucci, I., & Apai, D. 2015, *The Astrophysical Journal*, 814, 130, doi: [10.1088/0004-637X/814/2/130](https://doi.org/10.1088/0004-637X/814/2/130)
- Navarro, J. F., Frenk, C. S., & White, S. D. M. 1996, *The Astrophysical Journal*, 462, 563, doi: [10.1086/177173](https://doi.org/10.1086/177173)
- Ndugu, N., Abedigamba, O. P., & Andama, G. 2022, *Monthly Notices of the Royal Astronomical Society*, 512, 861, doi: [10.1093/mnras/stac569](https://doi.org/10.1093/mnras/stac569)
- Newton, E. R., Mondrik, N., Irwin, J., Winters, J. G., & Charbonneau, D. 2018, *The Astronomical Journal*, 156, 217, doi: [10.3847/1538-3881/aad73b](https://doi.org/10.3847/1538-3881/aad73b)
- Nielsen, J., Gent, M. R., Bergemann, M., Eitner, P., & Johansen, A. 2023, *Astronomy & Astrophysics*, 678, A74, doi: [10.1051/0004-6361/202346697](https://doi.org/10.1051/0004-6361/202346697)
- Phan, D., Pradhan, N., & Jankowiak, M. 2019, *Composable Effects for Flexible and Accelerated Probabilistic Programming in NumPyro*, doi: [10.48550/arXiv.1912.11554](https://doi.org/10.48550/arXiv.1912.11554)
- Pinsonneault, M. H., Elsworth, Y. P., Tayar, J., et al. 2018, *The Astrophysical Journal Supplement Series*, 239, 32, doi: [10.3847/1538-4365/aaebfd](https://doi.org/10.3847/1538-4365/aaebfd)
- Popinchalk, M., Faherty, J. K., Kiman, R., et al. 2021, *The Astrophysical Journal*, 916, 77, doi: [10.3847/1538-4357/ac0444](https://doi.org/10.3847/1538-4357/ac0444)
- Price-Whelan, A., Sipőcz, B., Lenz, D., et al. 2020, *adrn/gala: v1.3*, Zenodo, doi: [10.5281/ZENODO.4159870](https://doi.org/10.5281/ZENODO.4159870)
- Price-Whelan, A. M. 2017, *The Journal of Open Source Software*, 2, 388, doi: [10.21105/joss.00388](https://doi.org/10.21105/joss.00388)
- Prusti, T., Bruijne, J. H. J. d., Brown, A. G. A., et al. 2016, *Astronomy & Astrophysics*, 595, A1, doi: [10.1051/0004-6361/201629272](https://doi.org/10.1051/0004-6361/201629272)
- Queiroz, A. B. A., Anders, F., Santiago, B. X., et al. 2018, *Monthly Notices of the Royal Astronomical Society*, 476, 2556, doi: [10.1093/mnras/sty330](https://doi.org/10.1093/mnras/sty330)
- Queiroz, A. B. A., Anders, F., Chiappini, C., et al. 2020, *Astronomy & Astrophysics*, 638, A76, doi: [10.1051/0004-6361/201937364](https://doi.org/10.1051/0004-6361/201937364)
- . 2023, *Astronomy & Astrophysics*, 673, A155, doi: [10.1051/0004-6361/202245399](https://doi.org/10.1051/0004-6361/202245399)
- Reid, I. N., Hawley, S. L., & Gizis, J. E. 1995, *The Astronomical Journal*, 110, 1838, doi: [10.1086/117655](https://doi.org/10.1086/117655)
- Ricker, G. R., Winn, J. N., Vanderspek, R., et al. 2014, *Journal of Astronomical Telescopes, Instruments, and Systems*, 1, 014003, doi: [10.1117/1.JATIS.1.1.014003](https://doi.org/10.1117/1.JATIS.1.1.014003)
- Robitaille, T. P., Tollerud, E. J., Greenfield, P., et al. 2013, *Astronomy & Astrophysics*, 558, A33, doi: [10.1051/0004-6361/201322068](https://doi.org/10.1051/0004-6361/201322068)
- Rocha-Pinto, H. J., Flynn, C., Scalo, J., et al. 2004, *Astronomy and Astrophysics*, 423, 517, doi: [10.1051/0004-6361:20035617](https://doi.org/10.1051/0004-6361:20035617)
- Sagear, S., & Ballard, S. 2023, *Proceedings of the National Academy of Sciences*, 120, e2217398120, doi: [10.1073/pnas.2217398120](https://doi.org/10.1073/pnas.2217398120)
- Sagear, S., & Price-Whelan, A. 2024, *ssagear/zoomies: v0.1*, Zenodo, doi: [10.5281/zenodo.10806816](https://doi.org/10.5281/zenodo.10806816)
- Silva Aguirre, V., Davies, G. R., Basu, S., et al. 2015, *Monthly Notices of the Royal Astronomical Society*, 452, 2127, doi: [10.1093/mnras/stv1388](https://doi.org/10.1093/mnras/stv1388)
- Smith, R., Flynn, C., Candlish, G. N., Fellhauer, M., & Gibson, B. K. 2015, *Monthly Notices of the Royal Astronomical Society*, 448, 2934, doi: [10.1093/mnras/stv228](https://doi.org/10.1093/mnras/stv228)
- Soderblom, D. R. 2010, *Annual Review of Astronomy and Astrophysics*, 48, 581, doi: [10.1146/annurev-astro-081309-130806](https://doi.org/10.1146/annurev-astro-081309-130806)
- Soderblom, D. R., Duncan, D. K., & Johnson, D. R. H. 1991, *The Astrophysical Journal*, 375, 722, doi: [10.1086/170238](https://doi.org/10.1086/170238)
- Spitzer, Jr., L., & Schwarzschild, M. 1953, *The Astrophysical Journal*, 118, 106, doi: [10.1086/145730](https://doi.org/10.1086/145730)
- Stassun, K. G., Oelkers, R. J., Paegert, M., et al. 2019, *The Astronomical Journal*, 158, 138, doi: [10.3847/1538-3881/ab3467](https://doi.org/10.3847/1538-3881/ab3467)
- Steinmetz, M., Zwitter, T., Siebert, A., et al. 2006, *The Astronomical Journal*, 132, 1645, doi: [10.1086/506564](https://doi.org/10.1086/506564)

- Stokholm, A., Aguirre Børsen-Koch, V., Stello, D., Hon, M., & Reyes, C. 2023, *Monthly Notices of the Royal Astronomical Society*, 524, 1634, doi: [10.1093/mnras/stad1912](https://doi.org/10.1093/mnras/stad1912)
- Strömberg, G. 1946, *The Astrophysical Journal*, 104, 12, doi: [10.1086/144830](https://doi.org/10.1086/144830)
- Tarter, J. C., Backus, P. R., Mancinelli, R. L., et al. 2007, *Astrobiology*, 7, 30, doi: [10.1089/ast.2006.0124](https://doi.org/10.1089/ast.2006.0124)
- Tayar, J., Claytor, Z. R., Huber, D., & Sadlers, J. v. 2022, *The Astrophysical Journal*, 927, 31, doi: [10.3847/1538-4357/ac4bbc](https://doi.org/10.3847/1538-4357/ac4bbc)
- Vallenari, A., Brown, A. G. A., Prusti, T., et al. 2023, *Astronomy & Astrophysics*, 674, A1, doi: [10.1051/0004-6361/202243940](https://doi.org/10.1051/0004-6361/202243940)
- Van Eylen, V., Albrecht, S., Huang, X., et al. 2019, *The Astronomical Journal*, 157, 61, doi: [10.3847/1538-3881/aaf22f](https://doi.org/10.3847/1538-3881/aaf22f)
- Vasiliev, E. 2019, *Monthly Notices of the Royal Astronomical Society*, 482, 1525, doi: [10.1093/mnras/sty2672](https://doi.org/10.1093/mnras/sty2672)
- Veyette, M. J., & Muirhead, P. S. 2018, *The Astrophysical Journal*, 863, 166, doi: [10.3847/1538-4357/aad40e](https://doi.org/10.3847/1538-4357/aad40e)
- Wielen, R. 1977, *Astronomy and Astrophysics*, 60, 263. <https://ui.adsabs.harvard.edu/abs/1977A&A....60..263W>
- Winter, A. J., Kruijssen, J. M. D., Longmore, S. N., & Chevance, M. 2020, *Nature*, 586, 528, doi: [10.1038/s41586-020-2800-0](https://doi.org/10.1038/s41586-020-2800-0)
- Zhao, G., Zhao, Y.-H., Yao-Quan, C., Jing, Y.-P., & Deng, L.-C. 2012, *Research in Astronomy and Astrophysics*, 12, 723, doi: [10.1088/1674-4527/12/7/002](https://doi.org/10.1088/1674-4527/12/7/002)
- Zink, J. K., Hardegree-Ullman, K. K., Christiansen, J. L., et al. 2023, *The Astronomical Journal*, 165, 262, doi: [10.3847/1538-3881/acd24c](https://doi.org/10.3847/1538-3881/acd24c)

APPENDIX

A. RELATIVE AGE COMPARISONS

Throughout this work, we state that dynamical stellar age predictions may be interpreted as absolute ages as long as the calibration sample $\ln J_z$ distribution overlaps with the prediction sample $\ln J_z$ distribution. We perform a preliminary check for this statement. We begin with artificially reducing the RGB calibration sample by removing all stars to the right of the line $age = 7.5 \times \ln J_z - 12$. We do this to ensure that the natural slope of the age– $\ln J_z$ relation is preserved, while ensuring only the smallest $\ln J_z$ values remain in this calibration sample. The original and reduced calibration samples are shown in Figure 12.

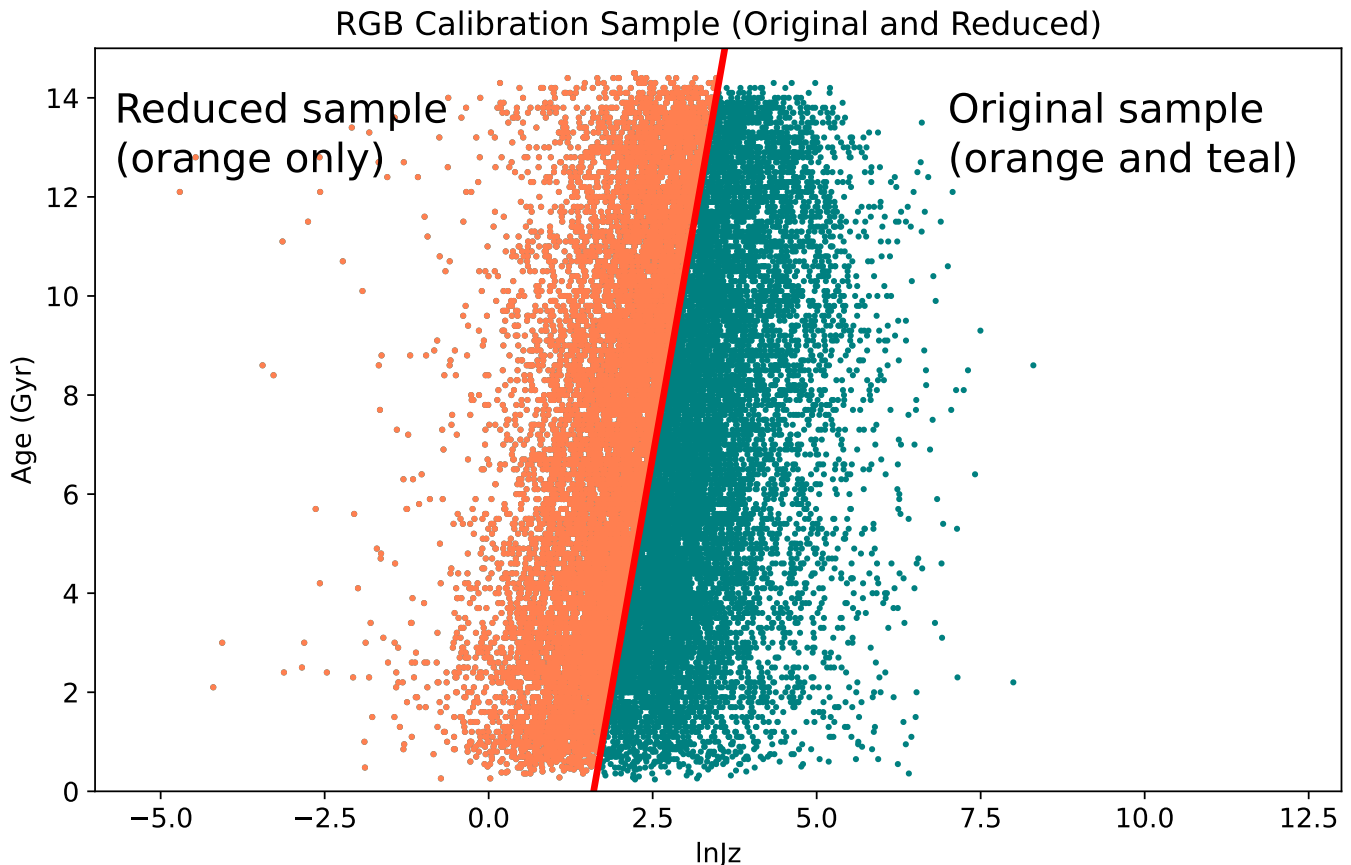


Figure 12. Original and reduced RGB calibration samples. The original RGB calibration sample is represented by all points (both orange and teal). The orange points only represent the reduced calibration sample: stars in the RGB calibration sample that lie left of the line $age = 7.5 \times \ln J_z - 12$ (red).

We then perform the age– $\ln J_z$ spline calibration process described in Section 3 using the reduced calibration sample. We generate age predictions for six selected $\ln J_z$ values using the new reduced age– $\ln J_z$ spline model, and we compare these age predictions with age predictions generated with the original age– $\ln J_z$ spline model. In Figure 13, we show a comparison of the two age predictions for six values of $\ln J_z$.

We do find that the age predictions appear similar for $\ln J_z$ values that are represented in both calibration samples ($\ln J_z$ values of 0 and 1), but they differ for $\ln J_z$ values where only one calibration sample is defined ($\ln J_z$ values of 2 and above). However, as expected, the relative ages match (i.e. a larger $\ln J_z$ value results in an overall older age prediction in both cases).

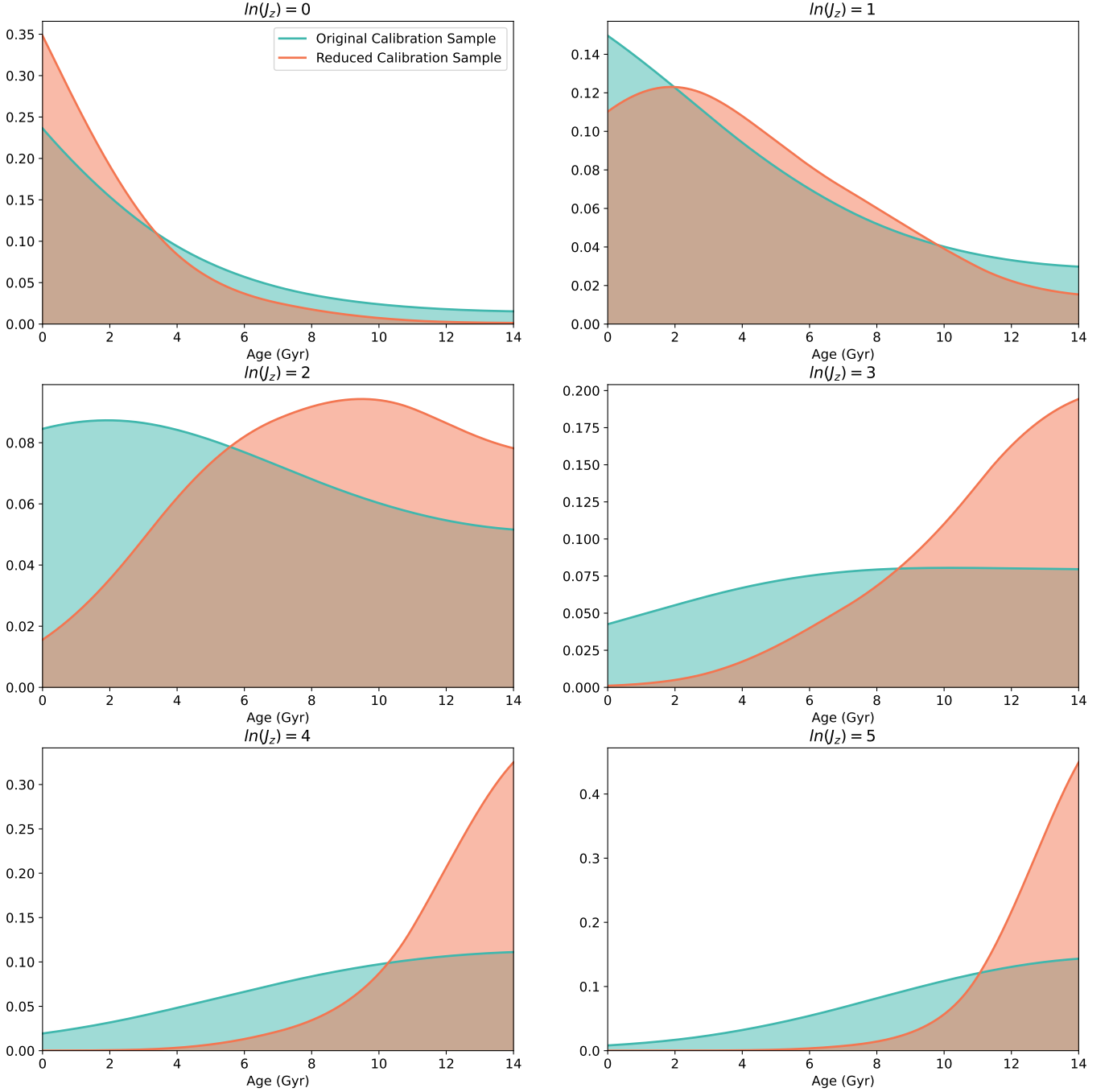


Figure 13. Comparison between original RGB age predictions (orange) and reduced RGB age predictions (teal) for six test values of $\ln J_z$. For the values of $\ln J_z$ which are well-represented by both the original and reduced calibration sample ($\ln J_z = 0$ and $\ln J_z = 1$), both age predictions appear similar. For larger values of $\ln J_z$ which are not well-represented in the reduced calibration sample, the absolute age predictions differ more significantly, while the relative age rankings remain consistent.

B. IMPACT OF GALACTIC MODELS ON AGE PREDICTION

It is necessary to choose a galactic potential model in order to calibrate the age–action relation, as described in Section 3. We perform a preliminary test to check the impact the choice of galactic model has on stellar age predictions. We compare age predictions for three extreme choices for galactic model, where the mass of the galaxy is composed entirely of a disk, bulge, or halo. We compare these resulting age predictions to the age predictions generated by the Milky

Way potential model and the RGB calibration sample used in this work. We calibrate three age–action spline models using the method described in Section 3, but changing only the galactic models. For the “All Disk” model, the galactic model is composed of a disk of $10^{10}M_{\odot}$, and no halo or bulge. For the “All Bulge” model, the galactic model is composed of a bulge of 50^9M_{\odot} , and no disk or halo. For the “All Halo” model, the galactic model is composed of a halo of $10^{11}M_{\odot}$, and no disk or bulge.

We choose six $\ln J_z$ test values between -2 and 3 to generate and compare age probability distributions for each model. In Figure 14, we show the age predictions using all three “test” galactic models, and the original Milky Way model used in the paper including a disk, bulge, and halo. We find that the entirely-disk and entirely-halo galactic potential models (orange and purple) produce age probability distributions very similar to that produced by the Milky Way model. The entirely-bulge potential model (red) differs more significantly, but critically, the ages rank appropriately (i.e. the age probability distributions always increase with increasing values of $\ln J_z$, no matter which galactic model is used).

We choose the most extreme galactic models for this demonstration, but in practice, it would be reasonable to choose a galactic potential model that resembles the Milky Way model. Therefore, we conclude that any reasonable choice of galactic model will at most slightly affect the age probability distributions. Even more extreme choices of galactic models are not likely to significantly impact stellar age predictions.

C. DEPENDENCE OF INTRINSIC AGE SCATTER ON STELLAR PARAMETERS

We conducted a preliminary test to check for any clear correlations between the intrinsic calibration age scatter and several stellar age parameters, such as stellar metallicity, $\log(g)$, alpha abundance, mass, radius, distance, and effective temperature. We begin by splitting up the RGB calibration sample into 37 arbitrary bins of $\ln J_z$, and calculating the standard deviation of stellar (calibration) ages within each bin. This metric serves as an approximation for the intrinsic scatter in age within each $\ln J_z$ bin. In Figure 15, we show the standard deviation of stellar ages, σ_{τ} , for the stars in each $\ln J_z$ bin vs. the midpoint of each $\ln J_z$ bin.

We then calculate the median of several stellar parameters for the calibration stars in each $\ln J_z$ bin. We use the stellar parameters published alongside the calibration ages in Stokholm et al. (2023). We plot σ_{τ} against the median stellar parameter value for ten different stellar parameters, shown in Figure 16. We do not find evidence for any clear correlations between intrinsic age variance and these stellar parameters. Indeed, action-driven ages are uniquely useful because they are based on stellar kinematics, and the dynamical age uncertainty is dominated by the intrinsic variance in the age calibration sample. Thus, the uncertainty in dynamical age predictions have little dependence on individual stellar properties.

D. OPEN CLUSTER AGE COMPARISONS

We present an extension of the open cluster dynamical age comparison described in Section 5.1. We consider the open clusters listed in Dias et al. (2021) with more than 100 listed members. Since the vast majority of open clusters in Dias et al. (2021) have $\tau < 1$ Gyr, we randomly select 15 clusters with $0 < \tau < 2$ Gyr and 25 clusters with $2 < \tau < 14$ Gyr according to Dias et al. (2021), with uniform probability within each bin. For each star associated with each chosen open cluster, we calculate $\ln J_z$ and the corresponding dynamical age probability distribution using the RGB-calibrated dynamical age model. In each subplot of Figure 17, we show the probability distribution of each star associated with each cluster (teal), along with the cluster age and 1σ age uncertainty presented in Dias et al. (2021) with the red lines and shaded regions, respectively.

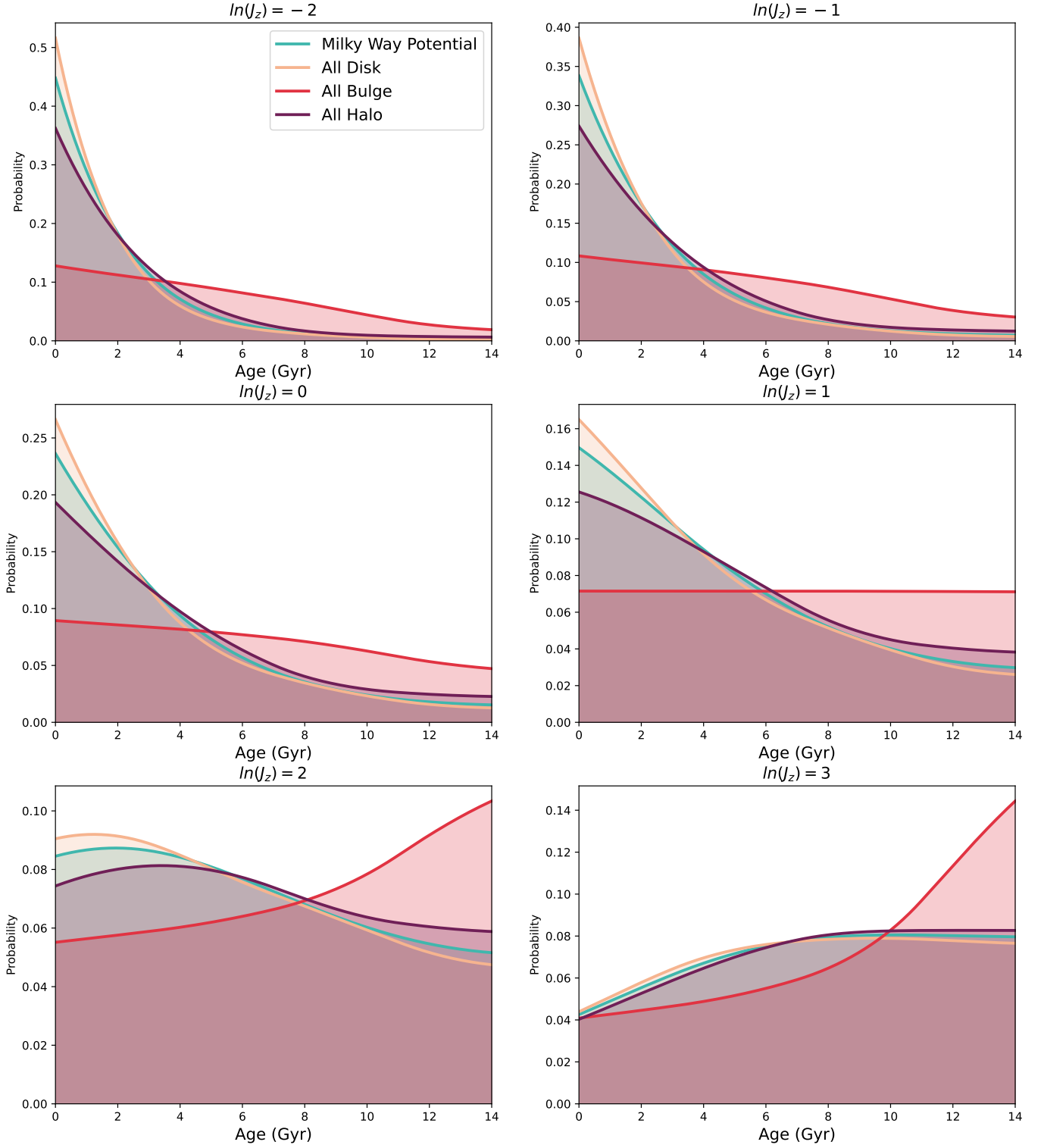


Figure 14. Comparison between age predictions (using the RGB calibration sample) generated with the Milky Way potential model (blue) vs. extreme custom galactic models, where the galaxy is composed entirely of a massive disk (orange), bulge (red), or halo (purple). Age predictions are shown for six test values of $\ln J_z$ between -2 and 3 .

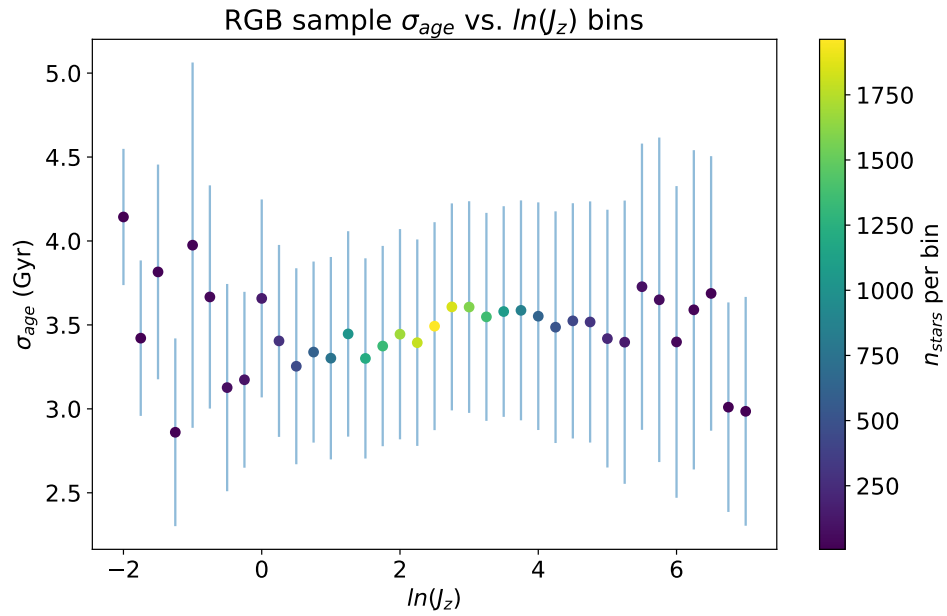


Figure 15. Standard deviation of stellar ages in 37 bins of $\ln J_z$ vs. midpoint of each $\ln J_z$ bin for the RGB calibration sample. The error bars on σ_τ represent the standard deviation of individual stellar age uncertainties for the stars in each bin. The color represents the number of stars included in each bin; the small sample size for bins with $\ln J_z < 0$ and > 5 likely contributes to the large scatter in σ_τ for low and high $\ln J_z$ bins.

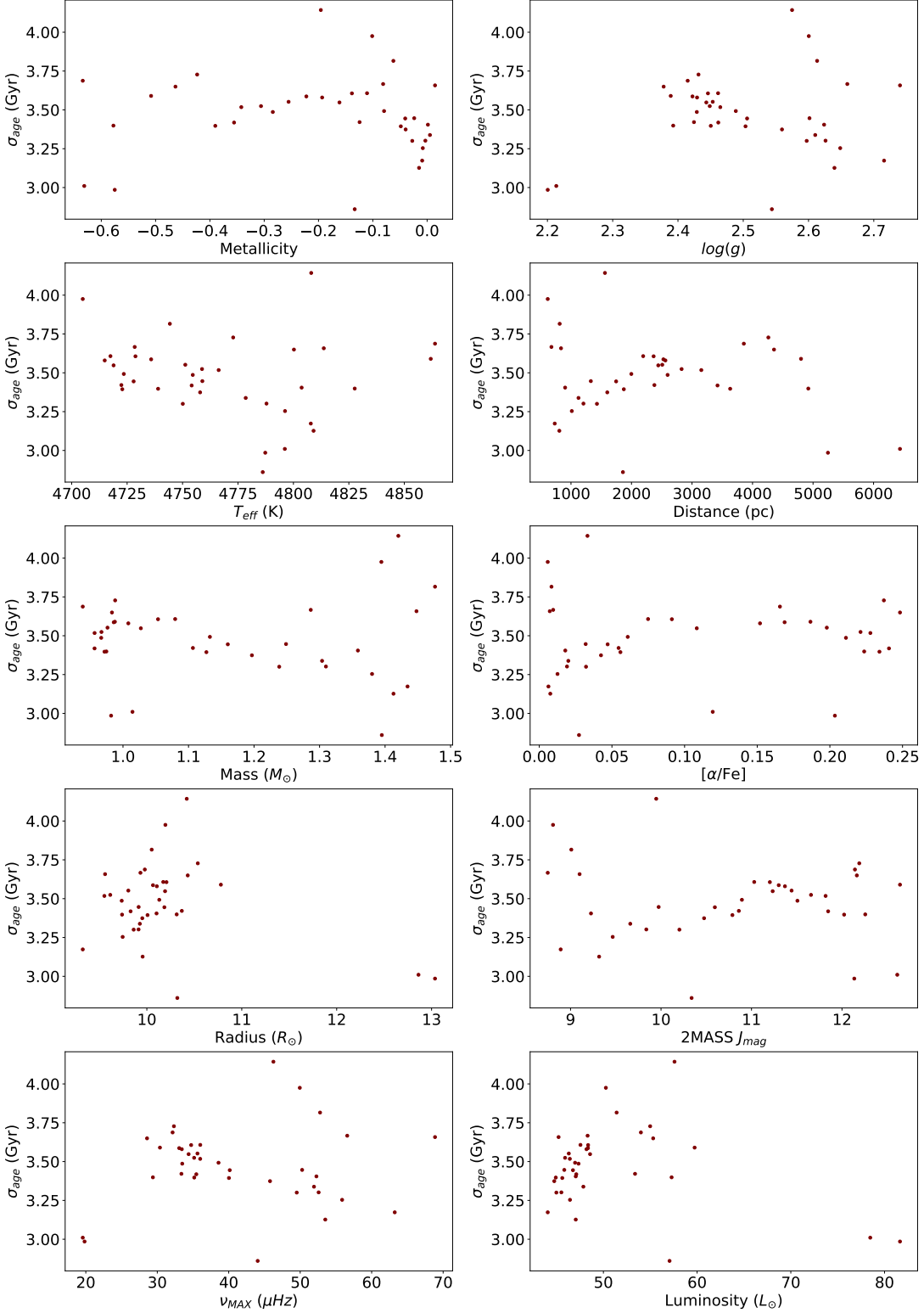


Figure 16. Standard deviation of RGB calibration ages in 37 $\ln J_z$ bins vs. median stellar parameter values in each bin (stellar metallicity, $\log(g)$, T_{eff} , distance, stellar mass, stellar radius, α/Fe , J -band magnitude, maximum frequency ν_{max} , and luminosity). All stellar parameters are published alongside the RGB calibration ages in [Stokholm et al. \(2023\)](#).

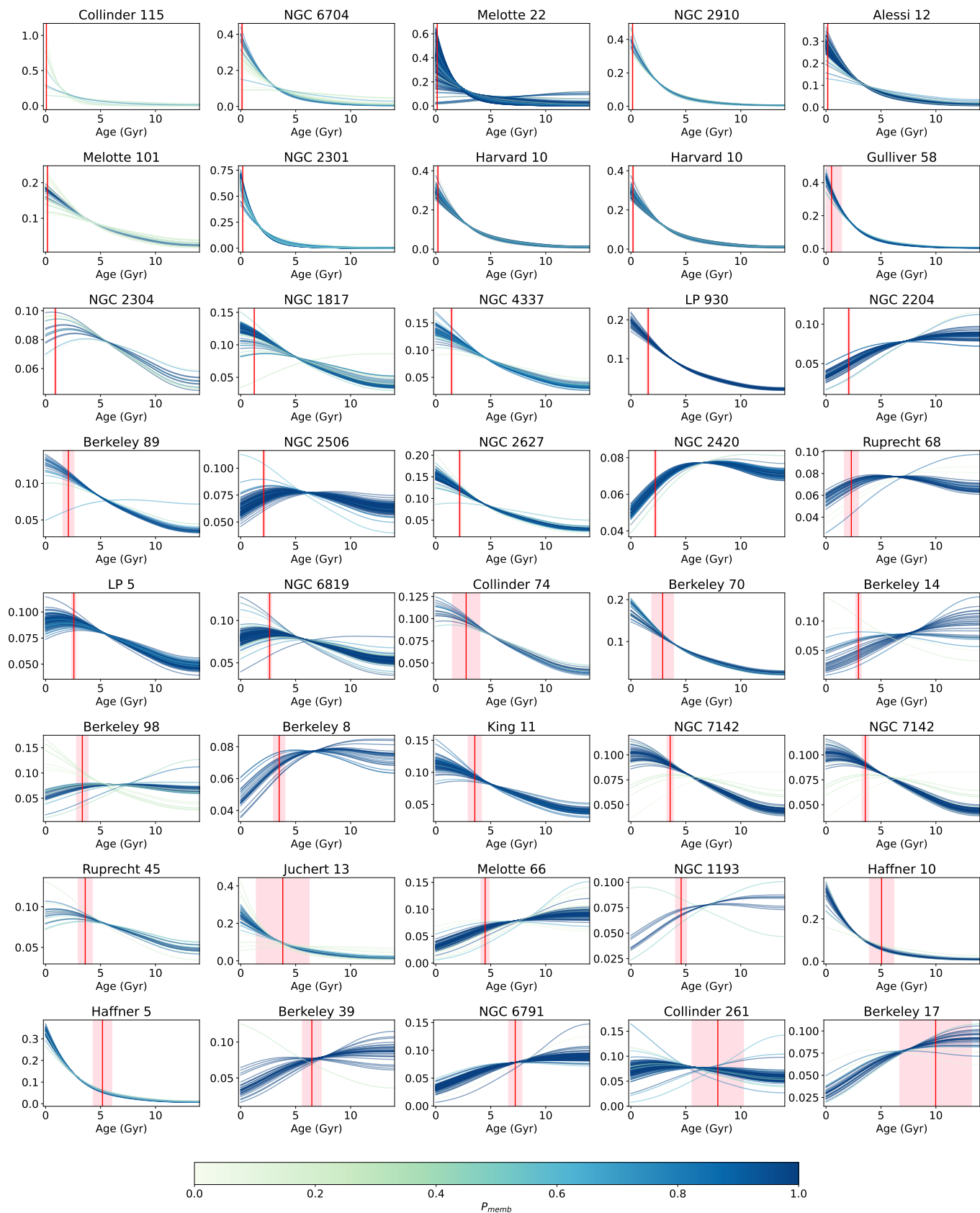


Figure 17. Age probability distributions for randomly selected open clusters from the [Dias et al. \(2021\)](#) sample. 15 clusters with $0 < \tau < 2$ Gyr and 25 clusters with $2 < \tau < 14$ Gyr according to [Dias et al. \(2021\)](#) were randomly selected to present a mix of young and old clusters. Each subplot shows the age probability distributions for each star associated with each cluster, with color denoting the membership probability according to [Dias et al. \(2021\)](#). The red vertical lines and shaded regions mark the cluster ages and 1σ uncertainties (respectively) presented in [Dias et al. \(2021\)](#).